

Investigation of Impurity Transport in DIII-D Diverted Negative Triangularity Plasmas

F. Sciortino^{1,2†}, N.T. Howard², T. Odstrčil³, M. Austin⁴, I. Bykov⁵, C. Chrystal³, J. D. Lore⁶, A. Marinoni², E.S. Marmar², O. Meneghini³, C. Paz-Soldan⁷, P. Rodriguez-Fernandez², S. P. Smith³, K. Thome³

¹ Max-Planck-Institut für Plasmaphysik, Boltzmannstraße 2, D-85748 Garching, Germany

² Massachusetts Institute of Technology, Cambridge, MA, 02139, USA

³ General Atomics, P.O. Box 85608, San Diego, CA 92186-5608, USA

⁴ University of Texas at Austin, Austin, TX, USA

⁵ University of California–San Diego, 9500 Gilman Dr., La Jolla, California 92093-0417, USA

⁶ Oak Ridge National Laboratory, Oak Ridge, TN 37831, USA

⁷ Columbia University, New York, NY 10027, USA

Abstract. Tokamak operation at negative triangularity has been shown to offer high energy confinement without the typical disadvantages of edge pedestals [Marinoni *et al* 2021 Nucl. Fusion 61 116010]. In this paper, we examine impurity transport and radiation, demonstrating favorable behavior in DIII-D diverted negative triangularity experiments. Lack of central impurity accumulation and short impurity confinement times (compared to energy confinement times) are conjectured to be due to lack of a main-ion density pedestal. Bayesian inferences of impurity transport coefficients based on laser blow-off injections and forward modeling via the Aurora package [Sciortino *et al* 2021 Plasma Phys. Control. Fusion 63 112001] show high core diffusion and flat/hollow impurity profiles during the experimental ramps of neutral beam power. Inferred radial profiles of D and v are compared to neoclassical, quasilinear gyrofluid, and nonlinear gyrokinetic simulations, observing that reduced turbulence models capture heat better than particle transport. State-of-the-art gyrokinetic modeling compare favorably with measurements across multiple transport channels. Overall, these results suggest that divertor impurity seeding in diverted triangularity discharges may offer a path to a highly-radiative L-mode scenario with high core performance.

1. Introduction

The development of high-confinement (H-mode) regimes in tokamaks [1] has motivated both optimization of high-performance scenarios and research into their widely recognized disadvantages. The occurrence of Edge Localized Modes (ELMs) is among the most critical of these, since plasma-facing components are unlikely to be able to sustain these sudden bursts of energy at the scale of a fusion reactor. It also remains unclear whether the existence of high H-mode pedestals and their consequent small divertor heat flux width [2] is compatible with material limits. While several variants of H-mode regimes without ELMs have been

† Email: francesco.sciortino@ipp.mpg.de

developed, these tend to accumulate impurities near the magnetic axis or incur undesirable reductions in overall plasma performance.

Diverted negative triangularity plasmas have recently been investigated as a possible solution to the core-edge integration problem in tokamaks [3, 4]. First explored experimentally in TCV [5, 6], negative triangularity has now also been successfully tested at DIII-D [7], first in an inner-wall-limited configuration [8, 9] and then with a lower single null diverted shape [10, 11]. The latest experiments have pushed operation towards equilibrated ion and electron temperatures ($T_i \approx T_e$), with core Ion Temperature Gradient (ITG) modes dominating over Trapped Electron Modes (TEM). A database study of regimes without ELMs at DIII-D has recently highlighted that diverted negative triangularity plasmas have already achieved comparable normalized performance to other no-ELM regimes, while maintaining divertor-compatible conditions of high separatrix density and displaying weak power degradation [12]. However, absolute performance has so far been modest, due to operational machine limits.

Impurity transport plays a central role in motivating interest in negative triangularity ($\delta < 0$). Standard H-mode scenarios (that is, at $\delta > 0$) cannot typically achieve high core confinement without ELMs while avoiding core impurity accumulation. This correlation is effectively broken in diverted negative triangularity L-modes, displaying a decoupling of particle and heat transport channels. In this configuration, trapped particles spend more time in “good curvature” regions [10], leading to a stabilization of core Trapped Electron Mode (TEM) turbulence [13] and lower fluctuation amplitudes [14]. Shorter scrape-off-layer (SOL) connection lengths have also been observed to lead to a more quiescent plasma edge [15]. Divertor target heat flux widths have been found to be smaller than for typical H-mode $\delta > 0$ plasmas, although wider than typical L-modes [10]. Given the inherently-larger separatrix wetted area and ease of coil operation at larger major radii, a “power-handling-first” philosophy [4] motivates further experiments, data analysis, and simulations at $\delta < 0$, in order to confirm or disprove whether this scenario should be explored in a new dedicated device, and possibly a future reactor.

In this paper, we examine observations of core particle transport and radiation in the first diverted negative triangularity plasmas at DIII-D, run in the fall of 2019. We demonstrate a decoupling of heat and particle transport in these discharges leading to promising scaling of highly-radiative $\delta < 0$ L-mode scenarios. We find high-fidelity transport models to compare favorably with experimentally-inferred impurity transport coefficients, suggesting that current predictive modeling capabilities are appropriate for further $\delta < 0$ experimentation. For a complete description of these experiments, readers are referred to Ref. [10]. In Section 2 of this paper, we first discuss core radiated power variations during Neutral Beam Injection (NBI) power ramps and relate these to plasma performance. In Section 3 we then describe data analysis methods and signals used for the Bayesian inferences of experimental impurity transport presented in Section 4. In Section 5, the results of these experimental inferences are compared to neoclassical, quasilinear gyrofluid and nonlinear

gyrokinetic modeling. Section 6 puts our experimental and modeling results in perspective, before concluding in Section 7. A more detailed description of the methods and data analysis presented in this paper can be found in Ref. [16].

2. Description of Experiments

Fig. 1 shows time traces for important quantities describing three key DIII-D discharges discussed in this paper (#180520, #180526, #180530). DIII-D is a medium-sized, C-wall tokamak with $R = 1.77$ m and $a = 0.57$ m. Diverted $\delta < 0$ experiments were run with plasma current $I_p \approx 0.9$ MA and toroidal field $B_T = 2$ T. The developed plasma shape was up-down asymmetric, with upper *delta* of -0.4 and bottom $\delta = 0$. In shots #180526 and #180530, Electron Cyclotron Heating (ECH) provided 1.5 MW, with near-axis deposition, on top of the power from Neutral Beam Injection (NBI), which increased in discrete steps until reaching 13 MW. The remaining discharge (#180520) had no ECH and the NBI ramp was limited to a maximum of 10 MW. No β limit was encountered in these experiments,

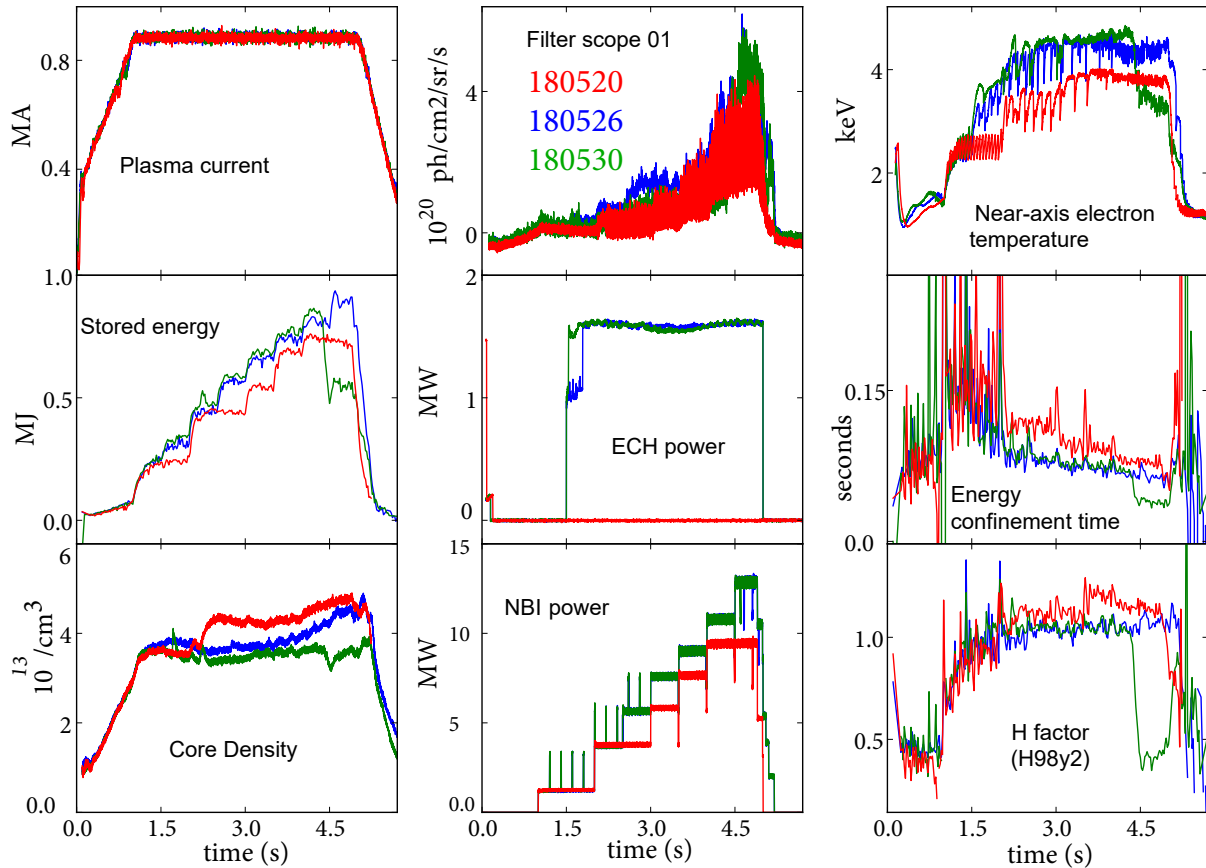


Figure 1: Evolution and comparison of the 3 DIII-D diverted negative triangularity discharges discussed in the text.

even when reaching $\beta_N \approx 3.1$, in agreement with theoretical predictions [3, 10]. Throughout these experiments, the H-mode transition was only observed in a single case, when one of the upper coils failed and the upper triangularity changed from -0.4 to -0.2 (the lower triangularity remaining near 0). This resulted in the stabilization of the infinite-n ballooning mode and thus enabled access to 2nd stability, where H-mode access is inhibited [11]. Shot #180520 (red in Figs. 1) is the discharge where this occurred, near 2.205 s. Fig. 2 illustrates the difference of plasma shapes (obtained via kinetic EFIT equilibrium reconstructions [17]) between the three discharges, taken at times of interest for the analysis later in this paper.

After the H-mode transition, the core density (bottom left panel in Fig. 1) of shot #180520 is seen to rapidly increase and then stabilize at a higher value. Note that density is also affected by fueling via NBI. The filterscope signals (top center panel in Fig. 1) show increasing D_α emissivity near the separatrix as auxiliary power is added, indicating a high degree of recycling from the edge. As discussed by Sareelma *et al.* [11], the H-mode plasma (red, #180520) displays small ELMs, whereas the L-mode cases show limit cycle oscillations (LCOs) that similarly result in rapid particle transport across the separatrix.

Energy confinement times (center right in Fig. 1) were near 70-120 ms (highest for #180520, after the transition to H-mode). Previous DIII-D inner-wall limited (IWL) discharges displayed little to no energy confinement degradation with auxiliary power [8].

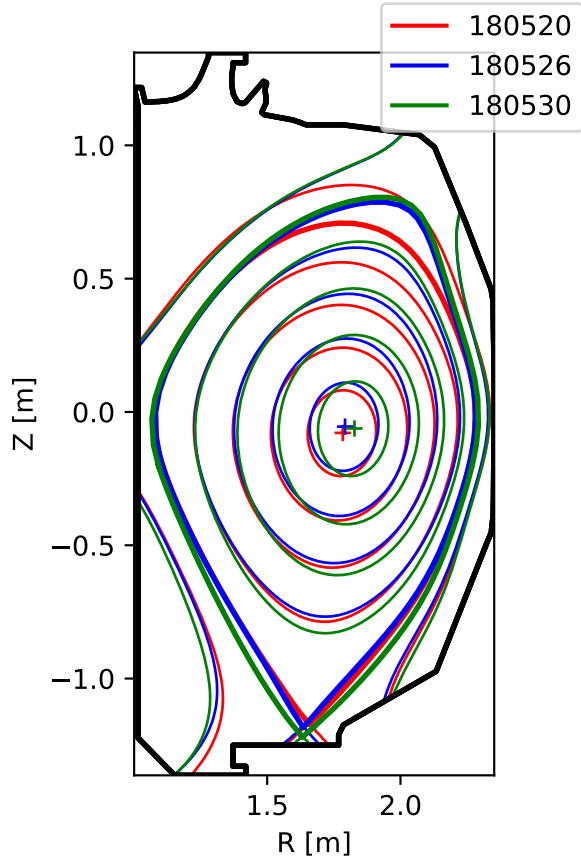


Figure 2: Comparison of plasma shapes from kinetic EFITs for the DIII-D discharges #180520 ($t = 2.501$ s), #180526 ($t = 2.75$ s), and #180530 ($t = 3.8$ s).

On the other hand, the presently discussed diverted discharges do present some degree of degradation during the NBI ramps, as discussed in Ref. [10]. This means that, as input heating power is increased, drift-waves are pushed above their critical gradients, resulting in higher turbulence growth rates. At diverted $\delta < 0$, this effect is weaker than expected from the ITER-89P scaling law [18, 10], which was created solely based on $\delta > 0$ plasmas. One may expect a reduction of power degradation with respect to IWL discharges because of lower C sputtering at the inner wall, leading to stronger ITG (stabilized via main ion dilution) [19, 20] as well as TEM (stabilized via collisionality) [21]. This would best be characterized as a change in impurity sources, rather than impurity transport. On the other hand, the average value of triangularity was also lower in IWL plasmas ($\delta_{av} \approx -0.4$, as opposed to -0.2 in the diverted shots), and this is likely to lead to significant differences in transport.

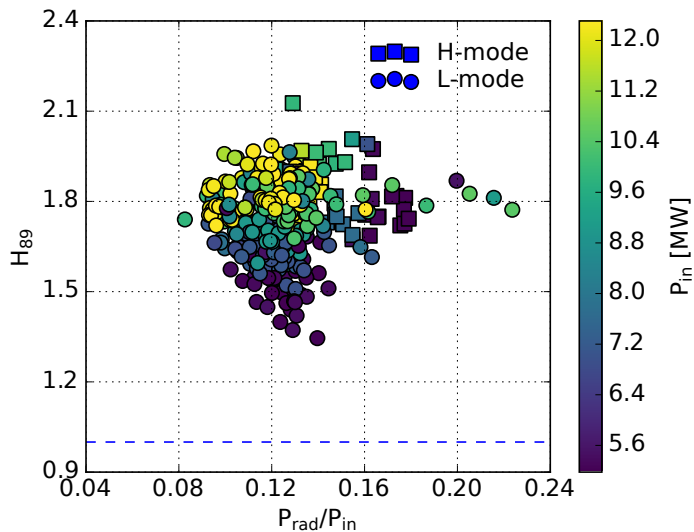


Figure 3: Variation of the L-mode H_{89} index with the ratio of power radiated in the confined plasma to the total input power.

Fig. 3 shows how confinement, as quantified via the H_{89} scaling for L-mode plasmas, varies with core radiated power, P_{rad} , from foil bolometers [22]. The latter was normalized by the total input power, computed as the sum of NBI, ECH and Ohmic power. The data points in Fig. 3 are from approximately 10 discharges from the same run day. H_{89} values have been found to be robustly near 1.8 at high NBI power (indicated by the colorbar). $H_{98,y2}$ values are consistently greater than 1 (*c.f.* Fig. 1), the value representing standard H-mode performance at $\delta > 0$ [23]. In Fig. 3, data points from the only H-mode case that was experimentally observed are distinguished using upward-pointing triangles, as opposed to lower-pointing ones for L-mode conditions, but the difference is relatively small.

We note that these plasmas had no divertor impurity seeding and maintained a remarkably low $Z_{eff} \approx 1.5$, resulting in low radiated power fractions of 10-20%. While the low Z_{eff} is already indicative of low impurity retention, one may want to directly assess to what extent this observation is due to lower wall C sources and/or to faster core impurity

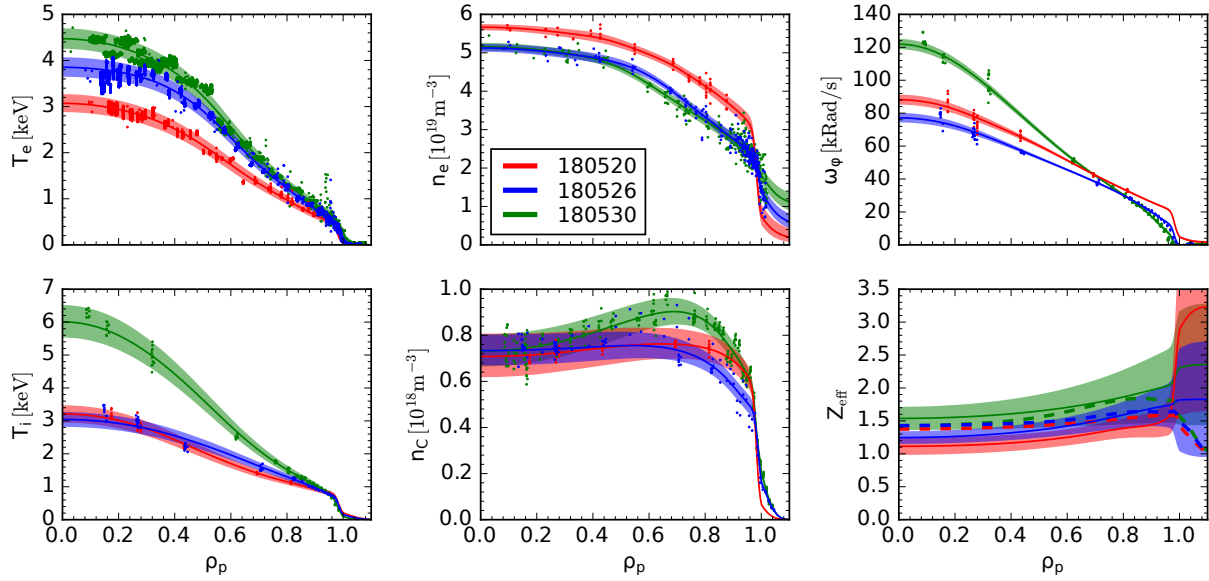


Figure 4: Kinetic profiles for the 3 diverted negative triangularity discharges discussed in this paper, averaged over a ± 50 ms time window near the LBO injection time: 2.501 s for the low-power H-mode case (#180520), 2.75 s for the low-power L-mode (#180526), and 3.8 s for the high-power L-mode (#180530).

transport. To address this question, Laser Blow-Off (LBO) injections were made in these experiments. In particular, here we examine the following in detail:

- An Al injection at $t = 2.501$ s in **#180520**, when only the 30L beam was operating, ≈ 300 ms after the discharge transitioned into H-mode (**low-power H-mode** case).
- A LiF injection at $t = 2.75$ s in **#180526**, when the 30L and 33L beams were operating. Only F ion densities were measured by the CER diagnostic (**low-power L-mode** case).
- An Al injection at $t = 3.8$ s in **#180530**, when the 30L, 33L, and 33R beams were all operational and high stored energies were achieved (**high-power L-mode** case).

Fig. 4 shows kinetic profiles for each of these discharges, averaged over ± 50 ms time windows near the times of LBO injections. Individual experimental data points are over-plotted in each panel, except when the profiles are inferred using line-integrated measurements. Ion temperature (T_i), toroidal rotation (ω_ϕ), and carbon density (n_C) are measured via CER, whereas electron temperature (T_e) and density (n_e) via Thomson scattering. Z_{eff} is from visible bremsstrahlung, with dashed lines showing the values estimated just from the measured carbon density, which accounts for most of the plasma dilution. Half of the CER channels were used for measurements of impurities injected via LBO. Comparing to the time traces in Fig. 1, we note that different NBI power is applied in each of these 3 time slices and this causes T_e (top-left panel) and T_i (bottom-left) to vary significantly. Electron density (top-center) is highest in the discharge that entered H-mode,

#180520. The plasma is seen to have a high rotation frequency (ω_ϕ) in #180530, when the NBI torque is near its maximum. Peaked toroidal rotation and ion temperature could both be contributors to the evidently hollow C profiles (bottom-center) seen in this case.

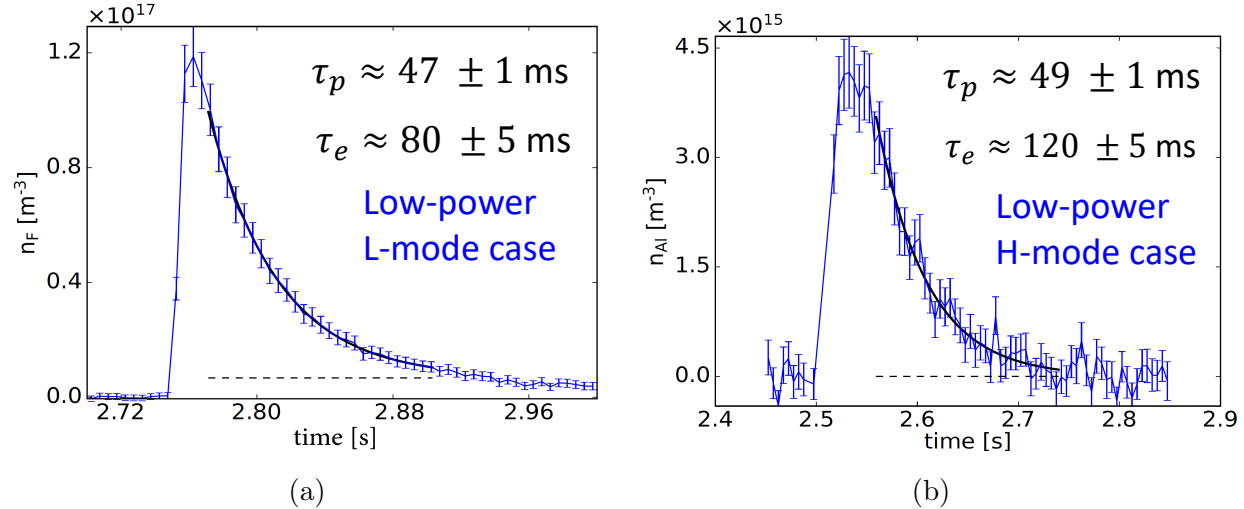


Figure 5: Signals from the CER T06 chord in (a) the low-power L-mode case (#180526, F) and (b) the low-power H-mode case (#180520, Al). Using exponential fits, impurity confinement times, τ_p , are quantified to be smaller than 50ms in both cases. Energy confinement times of ≈ 80 and 120 ms are also shown.

Fig. 5 shows signals from the CER T06 chord core measurements in shots (a) #180520 (viewing Al^{13+}) and (b) #180526 (viewing F^{9+}). Exponential fits to the decay phase allow quantification of the impurity confinement time, shown in the top-right corner. While these values should not be considered a truly global quantity and are only a rough measure of particle transport, they do offer the clear conclusion that impurity transport is fast and therefore favorable in these discharges. This is best observed by comparing values of $\tau_p \lesssim 50$ ms with the larger energy confinement times in the same discharges, $\tau_e \approx 70 - 100$ ms (*c.f.* Fig. 1). Such low values of τ_p/τ_e ratios are sometimes found in $\delta > 0$ L-modes, but usually not in H-modes. The decoupling of particle and heat transport observed in these negative triangularity plasmas is reminiscent of the I-mode regime [24, 25, 26]. In the next sections we delve more deeply into impurity transport by inferring radial profiles of transport coefficients for the three LBO injections listed above.

3. Experimental Data and Analysis Methods

In this section, we describe the experimental measurements and analysis techniques that have been used for inferences of radial impurity transport coefficients. Diagnostic forward models have been developed based on the Aurora package for particle transport, radiation,

and neutrals [27]§. All “synthetic diagnostics” have been implemented within the OMFIT **ImpRad** module, introduced in Ref. [27], which was used and expanded for most of the analysis described here.

3.1. Bayesian Inference

In the context of impurity transport inferences, **ImpRad** aims at finding D and v radial profiles that can accurately match experimental spectroscopic data. In order to do this, Aurora forward model simulations are run iteratively, varying a number of free parameters (including D and v splines values and knot locations), until reaching satisfying agreement with experimental measurements. Aurora’s 1.5D model solves coupled continuity equations for all charge states of a chosen impurity species over time and space (a 1D radial coordinate, mapping 2D flux surface volumes to 1D cylindrical geometry), accounting for both atomic physics (from the Atomic Data and Analysis Structure - ADAS) and transport (D and v profiles in space and time). The result of these simulations are density profiles for each charge state, emission for chosen transitions, and overall radiated power calculations, as illustrated in the diagram of Fig.1 of Ref. [27]. Although Aurora allows users to set different D and v for each charge state, in this work we make the common simplifying assumption of no transport dependence on Z . We note that, while poloidal impurity distributions are not yet directly modelled in Aurora, in-out asymmetries due to centrifugal effects [28] are accounted for after inferring flux-surface-averaged D and v , enabling effective comparison to *local* theoretical models [29, 30].

In inferring impurity transport coefficients, **ImpRad** iteratively compares experimental and simulation results, and can minimize their differences and quantify uncertainties via least-squares algorithms and/or Markov Chain Monte Carlo. In the present work, we adopt more advanced methods based on Importance Nested Sampling [31] using the **MultiNest** algorithm [32, 33]. The resulting framework is referred to as “fully-Bayesian” since it relies on sampling of free parameter values based on the definition of prior distributions that are entirely independent from experimental data.

The adopted inference scheme is analogous to the one developed for Alcator C-Mod research in Refs. [34, 35, 36]. Readers are referred to Ref. [35] (particularly the diagram in Fig. 4) for an overview of the adopted Bayesian methods and a discussion of relevant prior distributions. As in previous work, we choose to parametrize D and v profiles as splines, setting spline knots to be free using the scheme described in Appendix B of Ref. [36]. Additionally, a Gaussian feature has been added in the v profile near the separatrix in order to allow for effective representation of sharp pedestal features, setting the Gaussian amplitude, location, and width as free parameters.

The diagnostic forward models used here are the result of continuous development that already led to publications in Refs. [37, 38, 39]. In the following subsections we describe salient aspects of these models that have been expanded in the present work.

§ Aurora documentation can be found at <https://aurora-fusion.readthedocs.io/en/latest/>

3.2. LBO Source Functions

Fig. 6 shows time traces of spatially-integrated emission measured via an unfiltered visible fast (μs time resolution) camera [40] viewing the DIII-D LBO port during the three impurity injections of interest. In both cases with Al injections (#180520 and #180530) there is evidence of particles reaching the plasma several ms after the laser fired, as also observed in Extreme UltraViolet (EUV) spectroscopy of low charge states. This is likely the result of particle clusters not entirely ablated [41] and limits the accuracy of Al inferences near the pedestal, where D and v profiles are relatively sensitive to details in the source functions. F injection via LiF film ablation has not been found to have analogous problems.

3.3. EUV and SXR Signals

Data from the core-SPRED EUV spectrometer [42] have also been used to constrain both Al and F transport in the outer part of the plasma. We make use of ADAS Photon Emissivity Coefficients (PECs) produced from cross sections computed via R-matrix calculations and bin all emission within chosen wavelength regions. This allows for consideration of all atomic transitions whose energy falls within each bin, however many they may be. Tables 1 and 2 show the wavelength ranges that have been used in this analysis and the charge states that are found to give the strongest emissivity contributions.

However, matching multiple EUV lines simultaneously has been found to be challenging when considering their relative amplitudes. This is unlike in the Alcator C-Mod work in Ref. [36], where EUV line ratios from Ca LBO injections offered a useful constraint on near-edge transport. One possible explanation for the difficulties encountered in the present DIII-D analysis is that the F and Al atomic data from ADAS often have atomic energy levels that differ from those given by NIST [43], making it hard to accurately include all PEC contributions within chosen wavelength bins. Thus, we resort to normalizing each EUV line individually, i.e. ignoring line ratios and only considering line time histories. This offers a less powerful constraint, but greater resilience to inaccuracies in PECs, since

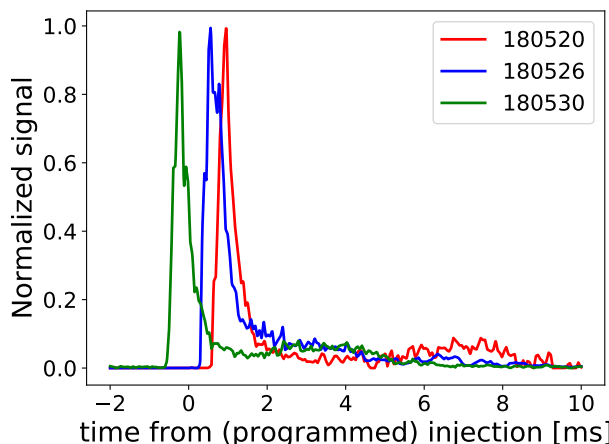


Figure 6: Effective source functions for LBO injections of F (for shot #180526) and Al (for shots #180520 and #180530) from the spatial integration of fast camera unfiltered signals.

Label	Measured λ [Å]	ADAS PEC range [Å]	Main contributors
F SPRED-0	464	464-467	F V
F SPRED-1	656	654-658	F V
F SPRED-2	645	647-648	F V
F SPRED-3	128	126.5-129	F VI & F VII
F SPRED-4	882	876-878	F VII
F SPRED-5	890	884-885	F VII

Table 1: EUV spectral lines used for the analysis of F LBO injections.

Label	Measured λ [Å]	ADAS PEC range [Å]	Main contributors
Al SPRED-0	282	270-288	Al VIII, IX, XII
Al SPRED-1	331	320-342.5	Al VII, VIII, IX, X, XI
Al SPRED-2	665	663-665	Al X
Al SPRED-3	549	547-548	Al XI
Al SPRED-4	567	564-566	Al X & Al XI

Table 2: EUV spectral lines used for the analysis of Al LBO injections.

time histories are dominated by ionization and recombination of charge states during LBO injections, rather than PEC dependencies on T_e .

We further constrain impurity transport using line-integrated SXR brightness with 125 μm -thick Be filter [44]. We choose not to use tomographic inversions to avoid systematic calibration errors that likely differ between different SXR detector arrays. Line-integrated brightness is normalized separately for each array. In order to reduce over-reliance on complex SXR atomic data accuracy, we make use of SXR data only from the initial signal rise after LBO injections. By doing so, we constrain transport in the decay phase of impurity signals only via local CER measurements, which have lower spatio-temporal resolution, but more validated atomic physics.

3.4. Multi-Impurity CER Analysis

For the first time, we apply a novel scheme to constrain impurity transport inferences from LBO injections making use of **simultaneous** C and Al/F measurements, using all available CER channels. Being intrinsic to DIII-D plasmas, C is almost always measured by the CER diagnostic in order to estimate ion temperature, T_i , and rotation frequency, ω_ϕ . T_i measurements from C^{6+} are used to constrain fitting of spectra of weaker intensity from non-perturbative LBO injections. The new scheme of this research uses C density measurements to constrain steady-state *density* profiles of low- Z impurities, rather than just temperature and rotation values. In practice, C transport is simulated using Aurora by initializing C^{6+} profiles in the plasma from the fitted CER values. We then apply a constant source of neutral

C in the SOL and allow it to evolve according to the chosen D , v , and background plasma profiles. When comparing C⁶⁺ profiles between Aurora and CER measurements, we ignore the first 50 ms of physical time after the start of the C injection to avoid an initial phase of profile stabilization. After this short time, comparison to C⁶⁺ experimental measurements offers valuable constraints on the v/D steady-state profile. We note that background plasma profiles are allowed to vary during this time and C⁶⁺ may be accumulating or decreasing in density over time, depending on the specific plasma scenario of interest.

The neoclassical transport is expected to display a significant dependence on Z , whereas turbulent transport likely has a negligible Z dependence within the achievable accuracy of this study. The variation of neoclassical diffusion with Z has been assessed with the NEO code [45] to be relatively small, so we take D to be the same for all the low- Z impurities. On the other hand, the present inferences of impurity transport allow convection to differ among ions near the magnetic axis and in the pedestal, but not at midradius. We set a single spline knot to be inside the $q = 1$ surface and have different values for each impurity (C + the species injected via LBO). Three more spline values of v outside of the $q = 1$ radius are set to be the same among ions. Furthermore, as mentioned in Section 3.1, we make use of a Gaussian feature in the pedestal to represent the sharp changes expected in this region. The amplitude of this Gaussian is set to be different for each species, with the amplitude for LBO impurities forced to be larger than for C, for which we use a prior $\mathcal{N}(0, 50)$ m/s. Since high-quality steady-state C measurements from CER are typically available in the pedestal, this constrains a minimum v/D for LBO-injected impurities.

This multi-impurity inference scheme has been found to be extremely effective in constraining reasonable solutions and is a key component of the results discussed in this paper. Fig. 7a shows an example of time histories for all the CER chords measuring F⁹⁺ in the low-power L-mode case (discharge #180526, $t \approx 2.75$ s). Here, black points with error bars represent experimental data and red lines show the result of the synthetic diagnostic based on Aurora when using Maximum A-Posteriori (MAP) parameters from an inference described in Section 4. Fig. 7b shows the analogous match for radial C profiles in the same discharge, with different panels corresponding to different time bins during the LBO injection. C densities are seen to be similar in each panel, as a result of quasi-steady conditions with no impurity accumulation in these $\delta < 0$ discharges. Matches of analogous quality were obtained for Al¹³⁺ data.

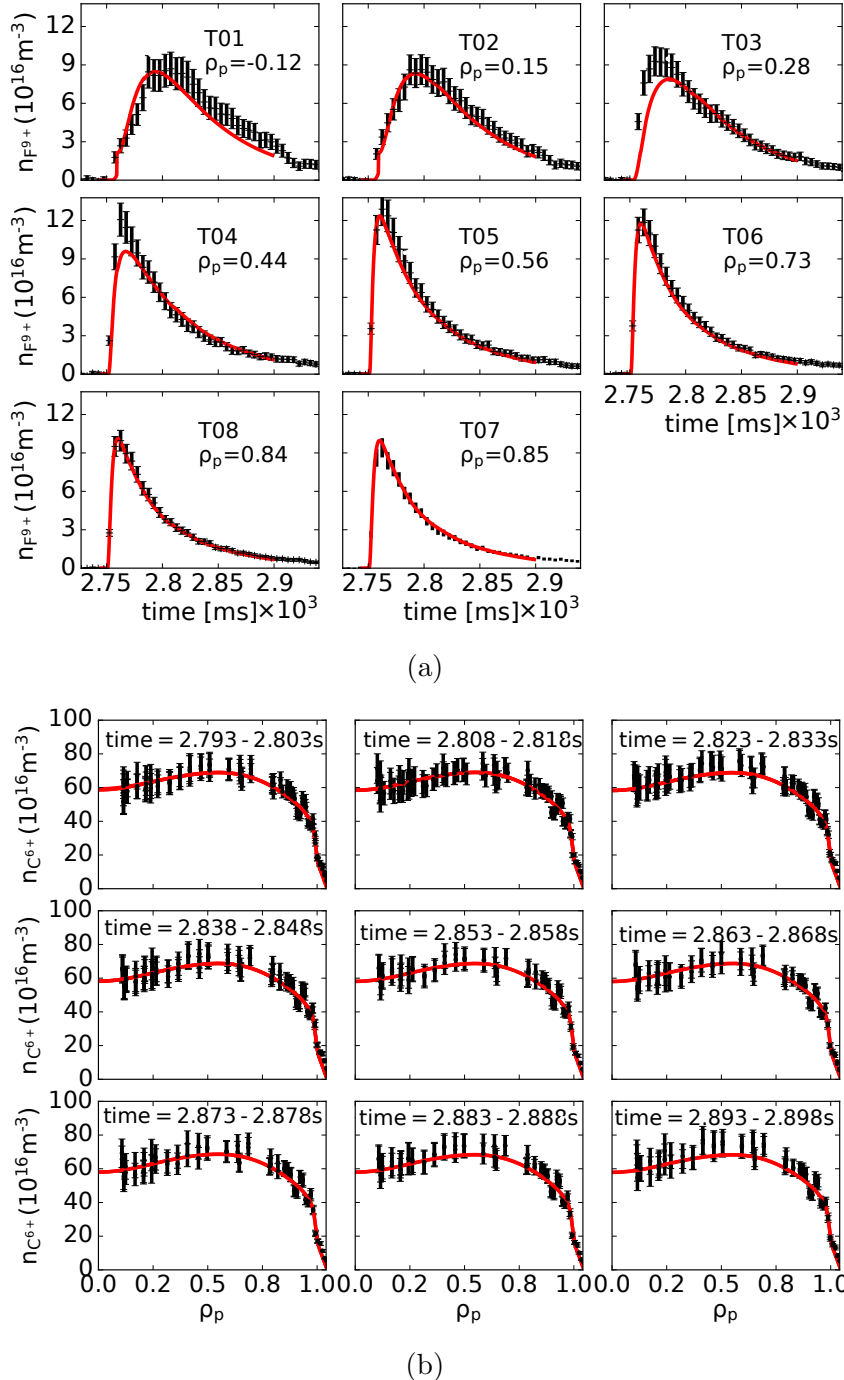


Figure 7: Match of experimental and modelled CER signals in the DIII-D $\delta < 0$ discharge #180526 for (a) time-dependent F^{9+} injected via LBO, and (b) intrinsic, steady-state C^{6+} . Modelled signals were obtained via Aurora and inferred MAP parameters for this discharge, as described in Section 4.

3.5. Background Neutral Density Predictions

Recent work on AUG [46] and Alcator C-Mod [36] has demonstrated that charge exchange (CX) of impurities with background D neutrals strongly affects charge state balance in the edge region. Here, as in Ref. [36], we make use of results from SOLPS-ITER [47, 48] simulations run with the EIRENE [49] Monte Carlo neutral code in order to estimate flux-surface-averaged deuterium neutral density profiles and assess their impact on impurity transport studies||. These simulations attempted to match experimental measurements of midplane electron density and temperature profiles, as well as divertor conditions. Unfortunately, such procedure has so far only been completed for two cases, the low-power H-mode (#180520, $t \approx 2.5$ s) and a low-power L-mode (#180533, $t \approx 2.3$ s). The latter is very similar to the repeated low-power L-mode condition in shot #180526, where we analyze the LBO injection at $t \approx 2.75$ s. In the absence of SOLPS-ITER results for the high-power L-mode case (#180530), we approximate this as having the same neutral density profiles as the low-power L-mode condition. We take the absolute amplitude of neutral densities to be a free parameter in inferences of impurity transport coefficients discussed in Section 4, with a log-normal prior that allows amplitude variations by up to a factor of 3, while neutral density *profile shapes* are fixed to those given by EIRENE.

Fig. 8 compares (a) charge state density profiles, and (b) line radiated power for two

|| Flux-surface averaging of neutral densities is justified by the fact that parallel impurity transport along closed field lines is faster than ionization events; readers are referred to Refs. [46] and [36] for detailed discussions on the subject.

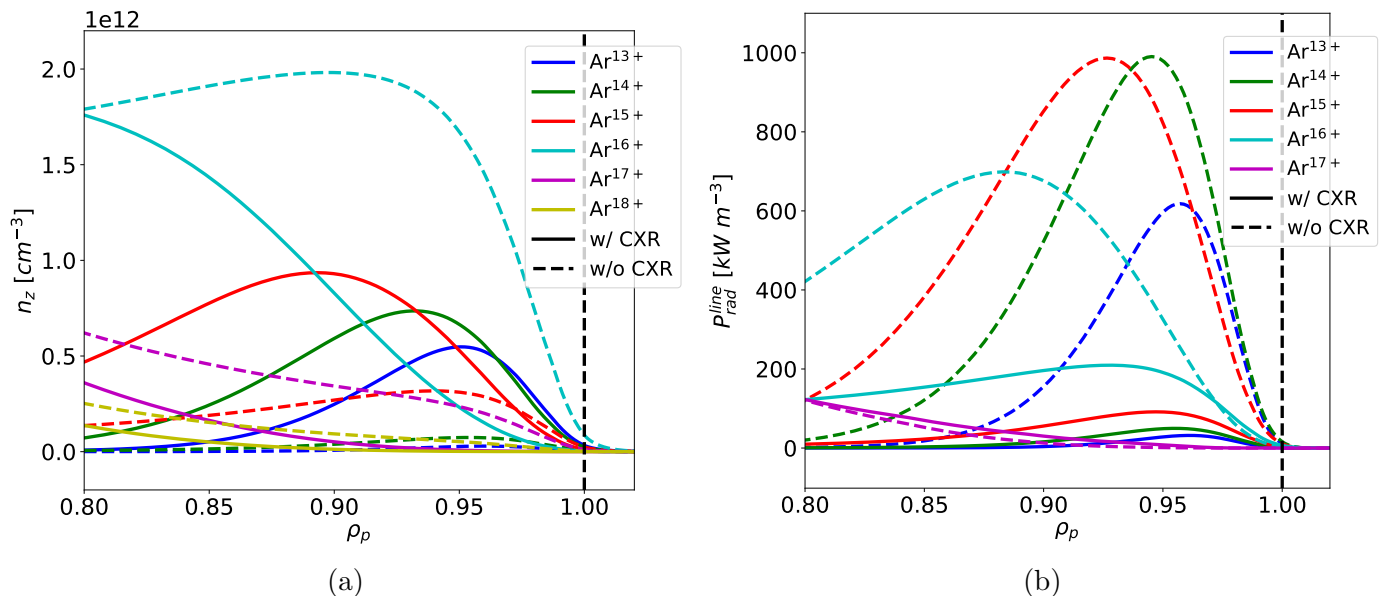


Figure 8: Charge state densities and line radiated power for Aurora simulations with and without CX in the DIII-D L-mode discharge #180533. Continuous lines show the result with CX, dashed lines without it.

Aurora Ar simulations for the high-power L-mode discharge (#180530) that are identical in all respects, except for the fact that one includes CX with background deuterium neutrals (from SOLPS-ITER), whereas the other does not. Realistic radial profiles of D and v have been used ($D = 1 \text{ m}^2/\text{s}$ and $v = 0 \text{ m/s}$ on the magnetic axis and rising sharply near the separatrix to -100 m/s), but the general observations described here are not affected by these choices. Values were normalized such that the He-like Ar density was the same between the two simulations on axis. The results in Fig. 8 are entirely analogous to those in Fig. 5 of Ref. [36], where similar results were shown for an Alcator C-Mod I-mode discharge. C-Mod plasmas typically have densities that are higher by up to one order of magnitude, and hence one naturally expects lower neutral penetration. Nonetheless, Ref. [36] showed that CX with edge neutrals is very important to consider if one is to capture impurity transport physics near the separatrix. Unsurprisingly, this effect is even stronger in DIII-D plasmas (likely, in any existing tokamak with densities lower than C-Mod's), as shown in Fig. 8.

On DIII-D, CX between impurities and NBI neutrals can also, in principle, affect charge state balance (on top, of course, of the important effect of NBI via heating, current drive, torque, etc.). Dux *et al.* [46] recently showed that NBI neutrals on AUG have a much smaller impact than neutrals from the edge. In the present work, the same conclusion has been reached for DIII-D plasmas. In order to assess this effect, FIDASIM [50, 51] Monte Carlo simulations of NBI neutrals have been run for each active beam in all discharges of interest. Appendix B describes these FIDASIM simulations and the quantification of CX rates between NBI neutrals and impurities. Here, we only report the final outcome of this detailed study. As shown in Fig. 9 for the low-power L-mode case, where beams 30L and 33L were active, the total recombination rate of LBO impurities has been found to be significantly affected by NBI neutrals near the magnetic axis, but always remains much smaller than the local ionization rate. The same conclusion generally holds independently of impurity species and charge state of interest. This makes the impact of CX with NBI neutrals relatively weak

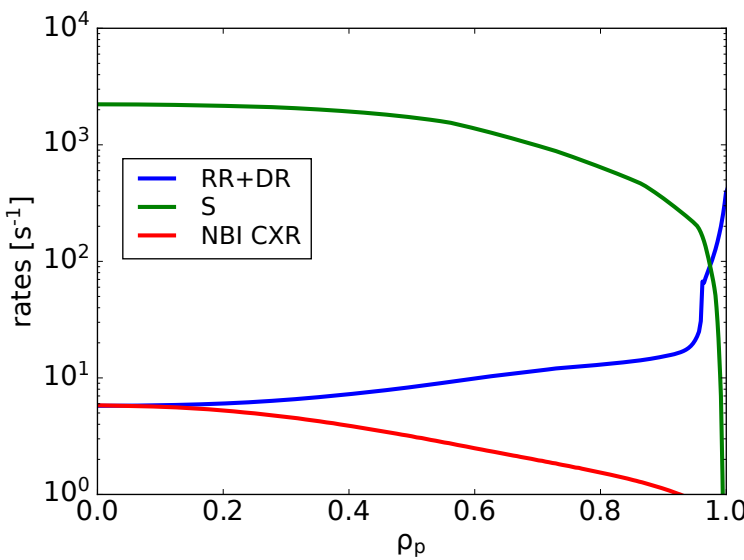


Figure 9: Comparison of radiative and dielectronic recombination (RR+DR), ionization (S), and CXR with NBI neutrals (NBI CXR) for F^{8+} in the low-power L-mode case, where beams 30L and 33L were active. Ionization dominates everywhere in the core, making the impact of NBI CXR relatively small.

(often negligible) in Aurora impurity transport simulations of DIII-D plasmas.

4. Impurity Transport Inferences

Fig. 10 compares the simultaneous inference of C and F transport coefficients near $t = 2.75$ s in the low-power L-mode case (#180526). Since this discharge had a sawtooth event occurring during the time range of evolution of the LBO injection, at $t \approx 2.784$ s, we also display the sawtooth mixing radius with thick, magenta, dashed lines, having estimated this location using fast Electron Cyclotron Emission (ECE) measurements [52]. Thinner magenta dash-dot lines in each panel represent the sawtooth *inversion* radius, approximated to be the mixing radius divided by $\sqrt{2}$ [53]. In each panel, inference results are shown with median values (continuous lines) surrounded by shaded regions representing the 1-99, 10-90, and 25-75 percentiles of the marginalized posterior distribution. We show only a single D radial profile (top-left panel) since this was set to be the same for the two impurity species. The Rv/D ratio was allowed to vary between the two ions in the region inside of the sawtooth mixing radius, and it is indeed found to be different, even changing sign, between F (green) and C (blue). The inferred pedestal pinches for the two species are not substantially different.

Fig. 11 compares the inferred F transport coefficients for this shot (#180526) with the results of neoclassical NEO [45, 54], quasilinear gyrofluid TGLF [55, 56, 57], and nonlinear gyrokinetic CGYRO [58] modelling. While a detailed comparison to theoretical models is left for Section 5, here we remark that steady-state F profiles (bottom-right panel) have gradients that are approximately similar to the rescaled time-averaged n_e profile (shown in grey), except inside of the sawtooth mixing radius (magenta dashed lines). The C^{6+} density profile with which this inference was constrained (see Fig. 4, bottom-center panel), also shows a profile shape that significantly differs from the n_e one inside of $\rho_p \approx 0.3$.

Figs. 12 and 13 show inferred transport coefficients for the low-power H-mode (#180520, $t \approx 2.5$ s) and high-power L-mode (#180530, $t \approx 3.8$ s) cases, respectively. Both of these inferences are based on LBO injections of Al, rather than F. It is possible that the presence of an Al^{10+} CX ($n = 14 - 12$) line at 4088 Å, almost degenerate with the CER Al^{12+} ($n = 12 - 11$) line of interest at 4084 Å, may affect CER measurements of Al^{13+} density. Since no effective subtraction methods for the Al^{10+} contribution are currently available, data points during the rise phase of the CER signal have been ignored in our inferences. Also, having observed a strong dependence of near-edge transport coefficients on details of the source functions, we choose to only focus on profiles inside of $\rho_p \approx 0.85$, particularly since the fast camera data (Fig. 6) suggest the existence of small Al LBO clusters in these injections. Fig. 12 and Fig. 13 display relatively flat or even hollow impurity density profiles, in agreement with the C profiles of Fig. 4. This hollowness does not appear to be entirely captured by NEO, TGLF, and CGYRO, although some encouraging trends can be observed, as further discussed in Section 5.

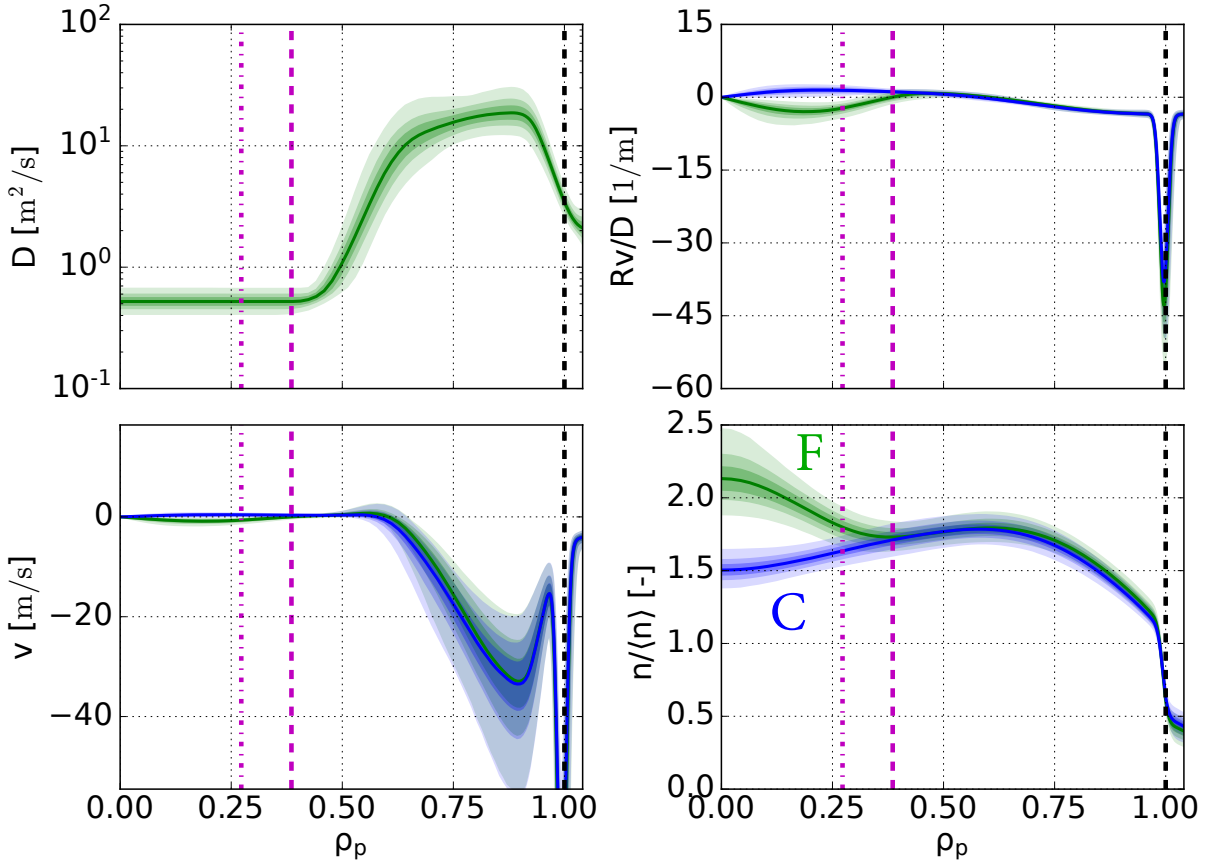


Figure 10: Inferred C (blue) and F (green) transport coefficients for the low-power L-mode case, shot #180526. The thick, magenta, dashed lines show the sawtooth mixing radius; the thinner dash-dotted lines represent the sawtooth inversion radius. Shared regions represent the 1-99, 10-90, and 25-75 percentiles of the marginalized posterior distribution.

5. Theoretical Transport Modeling

Section 4 presented inferred radial profiles of transport coefficients. In addition to the experimental results, Figs. 11, 12, and 13 also show predictions from NEO and TGLF SAT-2. Nonlinear gyrokinetic simulations with CGYRO have also been run at $r/a = 0.5$ and $r/a = 0.75$. Before describing the simulation setups in detail in the next sections, we describe some overall features of turbulence in the $\delta < 0$ discharges of interest.

Linear growth rate spectra agree on the observation that ITG turbulence is strongly dominant in both the $\delta < 0$ L-mode cases examined here. On the other hand, strong sensitivity to a/L_{T_e} and T_i/T_e in the low-power H-mode case suggests a non-negligible role of ETG in this scenario. Plasma collisionality has been found to only have a weak effect, consistent with the stabilization of TEM by $\delta < 0$ shapes that has been examined in previous works [13, 8]. The similar amplitude of $\gamma/k_\theta\rho_s$ at ion ($k_\theta\rho_s < 1$) and electron scales ($k_\theta\rho_s \gtrsim 1$) in the H-mode case suggests that multiscale interactions may be important in this condition,

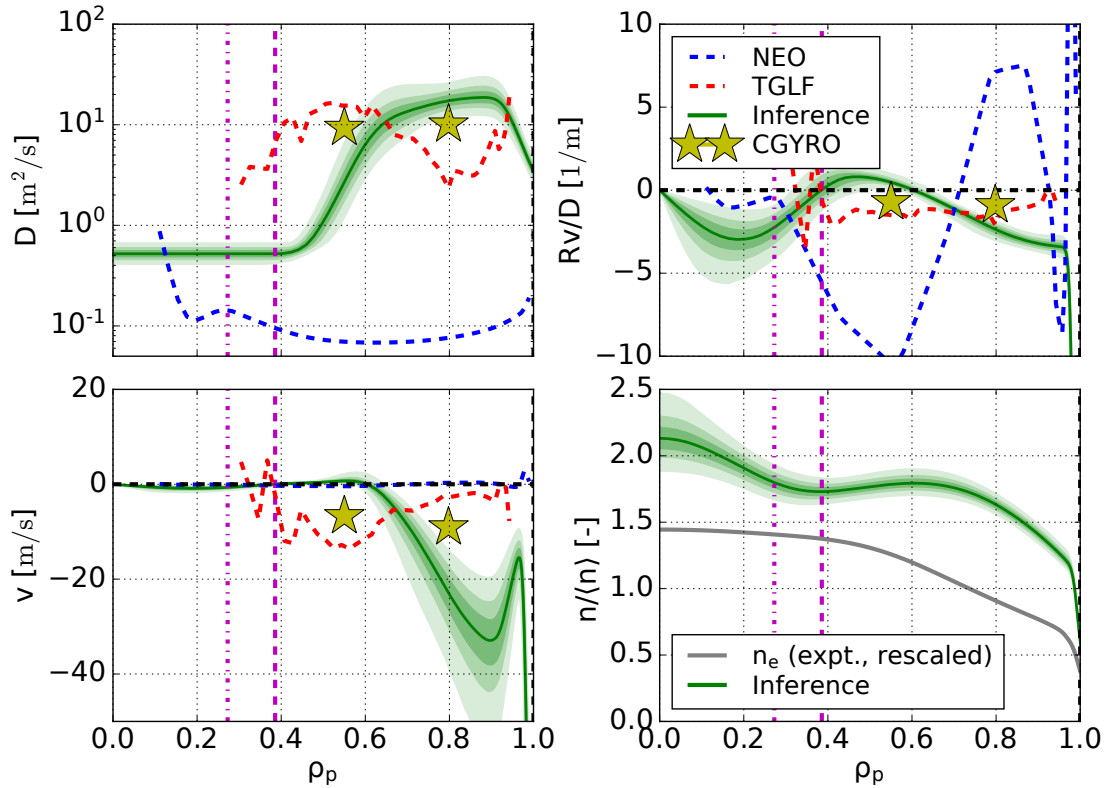


Figure 11: Inferred F transport coefficients for the low-power L-mode case, DIII-D shot #180526. The left column shows diffusion and convection, the right column their normalized ratio, Rv/D , and the approximate normalized steady-state profile of fully-stripped F. The rescaled time-averaged n_e profile is also shown for comparison. Results from NEO, TGLF SAT-2, and CGYRO are also displayed.

whereas they are unlikely to be significant in the L-mode cases.

5.1. Quasilinear Gyrofluid Turbulence Modeling

TGLF modeling is based on kinetic profiles obtained via TGYRO [59] (ion and electron) heat and (electron) particle flux matching. Results for each discharge are shown in Fig. 14. Left columns in each figure show T_i (top), T_e (middle) and n_e (bottom) profiles, with experimental fits shown as black dashed lines and TGYRO results obtained with TGLF SAT-0 (thin lines) and SAT-2 (thick lines) shown in red. SAT-0 is the original (oldest) TGLF saturation rule. SAT-2 is a recent revision and extension of SAT-1 [60] and it is therefore most interesting for validation studies at the time of writing.

The right columns in Fig. 14 show the ion heat flux, Q_i (top), the electron heat flux, Q_e (middle), and the convective heat flux component, $Q_{e,conv} := 1.5\Gamma_e T_e$ (bottom), which is

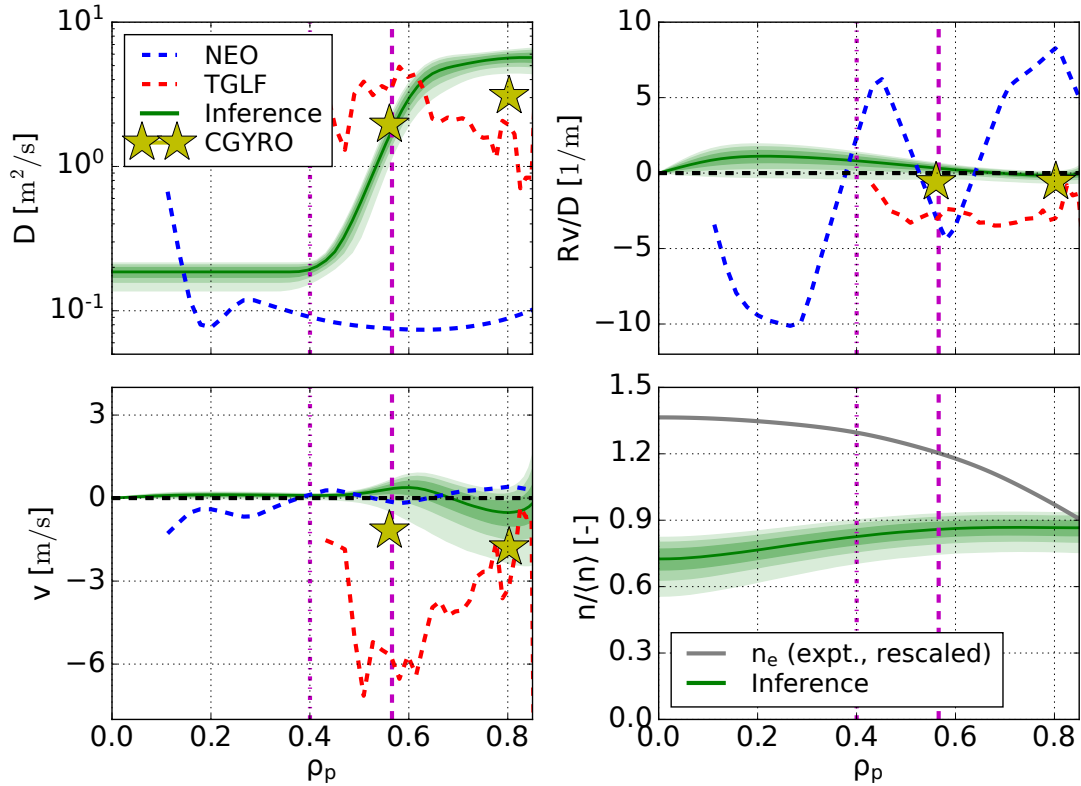


Figure 12: Inferred Al transport coefficients for the low-power H-mode case, DIII-D shot #180520. NEO, TGLF, and CGYRO results are also shown. Profiles are conservatively shown only inside of $\rho_p \approx 0.85$ because outer regions are affected by large uncertainties.

related to particle transport. As in the left column, black dashed lines show the experimental profiles, and (red and blue) line thickness indicates whether TGYRO was run with TGLF SAT-0 or SAT-2. Neoclassical fluxes from NEO (blue), mostly relevant for Q_i , are generally small compared to turbulent fluxes.

SAT-2 provides the best convergence further out in radius, displaying greater robustness at least up to $\rho_p \approx 0.9$. Both SAT-0 and SAT-2 are able to match power-balance heat and particle fluxes, computed via interpretative runs of TRANSP [61]. TGYRO operation using SAT-0 tends to result in kinetic profiles (T_i , T_e , and n_e) that are closer to the experimentally-measured values. While in discharges #180520 (top-left) and #180526 there is no strong difference in T_i and T_e matches, shot #180530 can only be flux-matched by SAT-2 if T_i is strongly reduced (by approximately a factor of 2) from the experimentally-measured values, well outside of uncertainties. For what concerns particle transport, SAT-2 is found to underestimate n_e in all discharges, whereas SAT-0 successfully reproduces the density profile in two of three cases. We note that the simultaneous match to Q_i , Q_e , and $Q_{e,conv}$ is easier for SAT-0 than SAT-2, as also evidenced by lower TGYRO residuals with SAT-0 ($\approx 10^{-3} - 10^{-4}$)

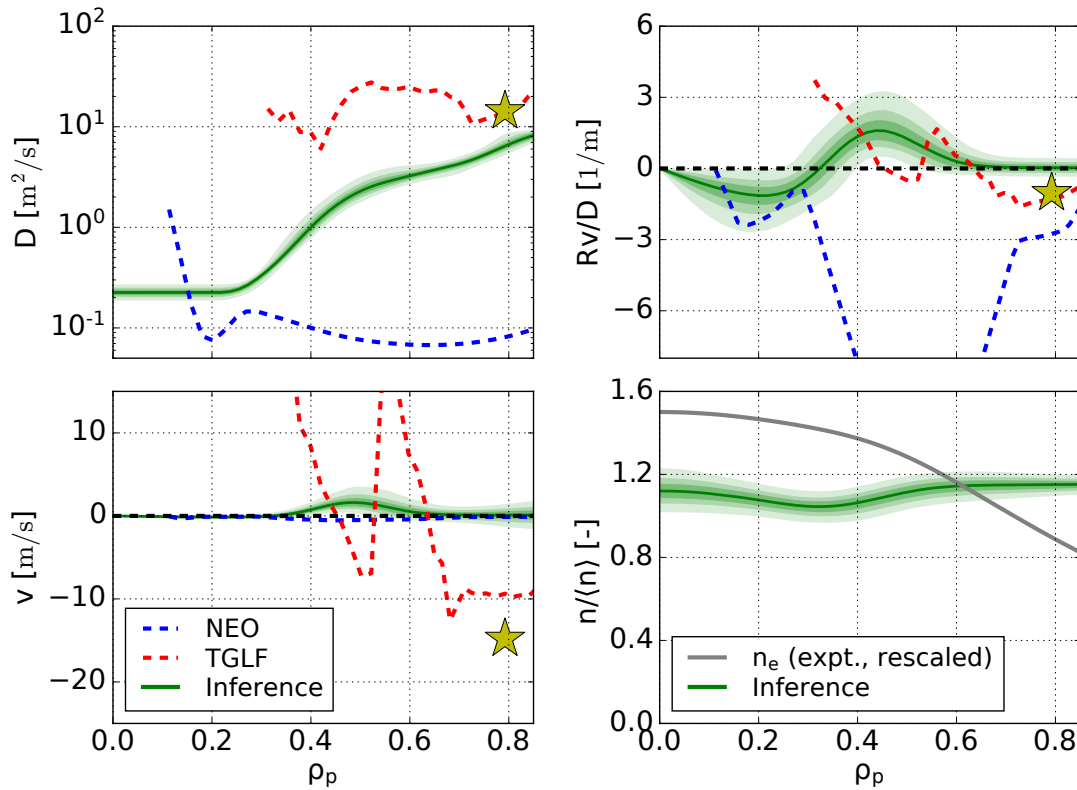


Figure 13: Inferred Al transport coefficients for the high-power L-mode case, DIII-D shot #180530. NEO, TGLF, and CGYRO results are also shown. As in Fig. 12, we only show results inside of $\rho_p \approx 0.85$ since regions further outside are affected by large uncertainties. **One more CGYRO case at $r/a = 0.5$ is currently being completed. CGYRO legend must also be added.**

than SAT-2 ($\approx 10^{-2} - 10^{-3}$). TGYRO convergence with SAT-2 was found to improve when increasing the number of poloidal modes (“NKY” parameter) from the default value (12) to 120. While this change does not lead to significant differences in heat transport, it appears to add smoothness to particle density and rotation profile predictions. Even so, it appears that as TGLF saturation rules become more sophisticated, D and v profiles lose some of the expected radial smoothness, as seen in Figs. 11, 12, and 13. A comparison of TGLF SAT-0, SAT-1 and SAT-2 predictions for D and v based on experimental profiles (from TRANSP, rather than TGYRO) is discussed in Appendix A.

Based on these observations, one may expect difficulties in predictions of impurity transport coefficients with SAT-2. However, this is the most physically comprehensive and advanced saturation rule in TGLF; it is therefore possible that the $\delta < 0$ cases discussed in this paper present outstanding challenges with respect to more standard tokamak scenarios. In what follows, unless otherwise specified, TGLF results refer to SAT-2 simulations.

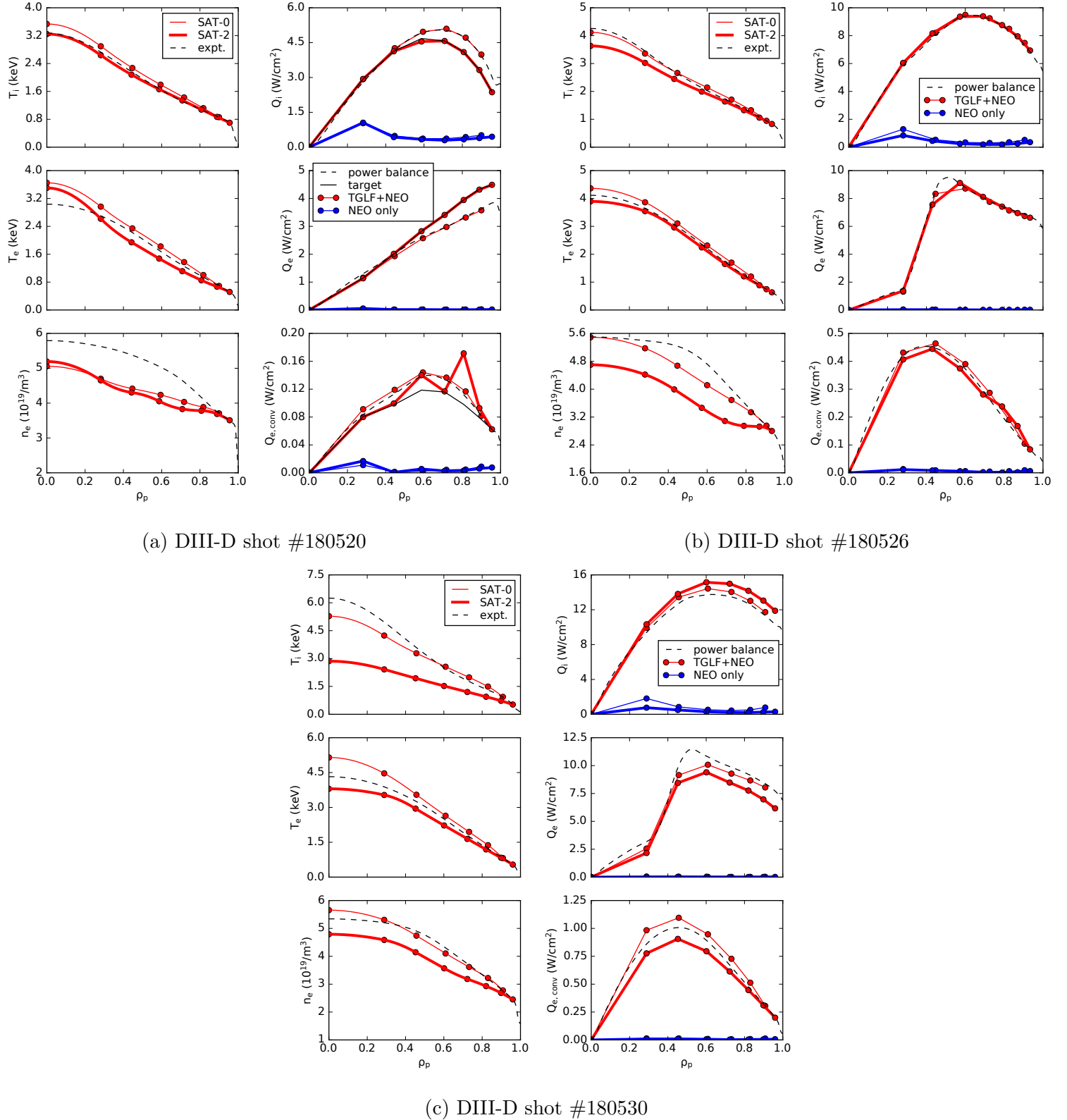


Figure 14: Summaries of TGYRO runs for the three $\delta < 0$ discharges examined in this paper. In each sub-figure, kinetic profiles are shown on the left and heat fluxes on the right. The convective electron heat flux, defined as $Q_{e,conv} := 1.5\Gamma_e T_e$, relates to particle transport.

5.2. Nonlinear Gyrokinetic Modeling

Approximately 25 nonlinear CGYRO simulations were performed to examine impurity transport in conditions that best reflect those found in the experiment. All runs included effects of electromagnetic turbulence ($\delta\phi$ and $\delta A_{||}$), $E \times B$ shearing and rotation effects, realistic geometry, and Sugama collisions [62]. Simulations performed at $r/a = 0.75$ utilized only 3 gyrokinetic species (deuterium, carbon, and electrons), whereas simulations performed at $r/a = 0.5$ included an additional fast deuterium species (4 total gyrokinetic species). At $r/a = 0.75$ the fast species was $\lesssim 2\%$ of the electron density and exhibited temperatures much closer to the thermal species, making it reasonable to neglect them to spare computing resources. The simulation domains were $L_x \times L_y \sim 100 \times 90\rho_s$ with a target radial grid spacing of $\Delta r/\rho_s = 0.33$, which resulted in approximately 336 radial modes in each simulation. Each simulation utilized resolutions of $n_\theta = 24$, $n_\chi = 24$, and $n_{energy} = 8$, with 16 toroidal modes spanning up to a $k_\theta\rho_s \sim 1.0$ in order to properly capture low-k turbulence such as ITG and TEM. As shown in previous works (e.g. Ref. [36]), turbulence at higher k-values is unlikely to have any effect on impurity transport. Simulations were run for typically $800 - 900 a/c_s$ with approximately $300 - 500 a/c_s$ time averaging to determine heat and particle fluxes.

Due to the strong dependence on ITG drives for all conditions studied, scans of a/L_{T_i} were performed around the experimental input gradients to attempt to match the experimental values of ion heat flux found in experiment, as quantified via TRANSP [61]. In practice, it was found that Q_i at all radial locations responded quite sensitively to changes in a/L_{T_i} , making the reproduction of experimental ion heat fluxes relatively straightforward. Modifications to the input a/L_{T_i} values were typically within 15% of the experimental value, generally within the 1σ experimental uncertainty in this quantity. The gradients that were found to best reproduce the experiment were considered ion heat flux-matched and used as the conditions to study trace impurity transport. Two trace species (F for the low-power L-mode, Al for the other two cases) were introduced into each of the simulated conditions at $10^{-6} \times n_e$, with two different values of gradient scale length, allowing one to easily extract trace impurity diffusion and convection from the slope and intercept of Γ/n vs. $-\nabla n/n$. The next section compares the calculated D and v values to experimentally-inferred profiles, as well as to TGLF quasilinear gyrofluid modeling.

5.3. Comparison to Experimental Impurity Transport

Figs. 11, 12, and 13 show comparable agreement between experiment and turbulence theory for the three examined cases. CGYRO is found to give estimates that are generally closer to experimental inferences. Convection is experimentally inferred to be small in the core of all three cases, with some degree of density profile hollowness, especially in the high-power L-mode case (#180530). We note that although it may seem that there exist strong disagreements in v values, convection is consistently found to be small by both theory and experiment, thus giving $v/D \lesssim 0$. This may be interpreted as successful validation of the

present theoretical turbulence models, within inescapable input uncertainties. Even in the high-power L-mode case, where $v \approx -15$ m/s at $r/a = 0.75$, the value of v/D remains small since D is quite large. **One more CGYRO run at $r/a = 0.5$ is currently being completed and will be included here before submitting to PPCF.**

Impurity transport coefficients in the low-power L-mode case (#180526, Fig. 11) agree relatively well between CGYRO and experiment at both the radial locations where simulations were run. TGLF, on the other hand, shows radial variations in both D and v that differ from experimental estimates. Issues in TGYRO flux-matching, discussed in Section 5.1, certainly affect the overall profile shapes. Nonetheless, TGLF Rv/D values are in relatively good agreement with CGYRO, with CGYRO predicting lower density peaking. We remark that TGLF Rv/D values of ≈ -1 are small compared to typical peaking in $\delta > 0$ discharges.

The low-power H-mode case (#180520, Fig. 12) shows good agreement between CGYRO and the experimental inference. In particular, CGYRO values of v are very close to 0, resulting in almost entirely flat impurity profiles, in agreement with the experimental result. TGLF seems to approximately capture the appropriate D and v amplitudes, although not the radial profiles. Moreover, TGLF Rv/D values correspond to strongly peaked impurity profiles at midradius, in clear disagreement with CGYRO and experimental estimates.

In Ref. [16], TGLF SAT-0 was shown to give a relatively good match in D in the high-power L-mode case (#180530), but Fig. 13 presents a more problematic comparison to experiment when using SAT-2. D is found to be larger than $10 \text{ m}^2/\text{s}$ in the range $0.4 < \rho_p < 0.85$, in disagreement with the experimentally-inferred results. It is encouraging, however, the D values at $\rho_p \approx 0.8$ are close between TGLF SAT-2, CGYRO, and experimental estimates. Rv/D values from both CGYRO and TGLF SAT-2 are near 0, in good agreement with the experimental inference, albeit TGLF's predictions evidently lack of radial smoothness.

The NEO results in Figs. 11, 12, and 13 are based on kinetic profiles obtained via TGYRO using TGLF SAT-2. Neoclassical transport coefficients in these figures display only some qualitative agreement with experiment near the magnetic axis, with the greatest deviation arguably seen in the low-power L-mode case (Fig. 11). In the high-power L-mode case (Fig. 13), v/D is well matched within uncertainties inside of $\rho_p \approx 0.3$, and D and v are within a factor of 2. In the low-power H-mode case (Fig. 12), D is also similar near the magnetic axis, but the NEO v/D values are quite large and negative. We note that a single sawtooth crash was present (and phenomenologically modelled with Aurora, as described in Ref. [27]) in the time range of interest in #180520 and #180526, whereas no sawteeth were present in #180530. In all cases, we find a sudden rise of neoclassical D in the range $0.1 \lesssim \rho_p \lesssim 0.15$ (outside of a few potato orbits from the magnetic axis, where neoclassical theory does not typically apply). This sharp feature is related to details of the rotation profile and not likely to be physical. We note that NEO modeling based on experimental profiles, rather than profiles obtained via TGYRO, can reproduce relatively well the experimental carbon density profile shapes (including hollowness) in Fig. 4, which are used as a constraint

in Al and F transport inferences in this work. Consequently, we conclude that NEO can appropriately model impurity peaking (or lack thereof) in these $\delta < 0$ discharges, although not in combination with TGYRO and TGLF SAT-2.

6. Discussion

In this paper, we have presented an investigation of impurity transport and radiation in recent DIII-D diverted negative triangularity discharges. Previous analysis on these experiments [10, 11] has been here complemented with both global and local metrics of impurity transport, highlighting favorable behavior of these plasmas that encourages further scenario development. Leveraging recently developed analysis and simulation tools, we have presented radial profiles of particle transport coefficients from experimental inferences based on Al and F LBO injections. Values of $Z_{eff} \approx 1.5$ measured in these experiments (Fig. 4) are remarkably low compared to previous IWL DIII-D $\delta < 0$ shots [8], consistently with the low measured C density and the rapid decay of CER signals following LBO injections (Figs. 5a and 5b). We note that DIII-D $\delta > 0$ discharges with comparable heat confinement typically have higher Z_{eff} and often present impurity density peaking, strong pedestal inward pinches, and long impurity confinement times.

All inferences have shown significant deviation of impurity profile shapes with respect to n_e density profiles. This suggests that models that set impurity density profiles as a constant fraction of the n_e profile often run into important inaccuracies.

The v/D constraint provided by C^{6+} density measurements is clearly effective, yet insufficient to separate the effects of D and v just inside of the separatrix, where ion scale turbulence is expected to be sub-dominant to neoclassical effects [63]. The clear dependence of near-edge D and v on details of the Al source time histories prevents their detailed examination in shots #180520 and #180530. Sensitivity tests have shown that reasonable variations of the source function do not affect inferred transport coefficients inside of $\rho_p = 0.85$ for these discharges, thus allowing more meaningful model comparisons in the core. Inferred transport coefficients for shot #180526 appear to be more robust to uncertainties in F source details up to near the separatrix. However, it is clear that the present data is inadequate for detailed validation of near-edge impurity transport. Nonetheless, one may evidently conjecture that the rapid impurity transport observed in DIII-D diverted $\delta < 0$ discharges is partly due to the lack of a strong particle transport barrier inside of the separatrix. The high core diffusion and low convection coefficients inferred in these discharges lead to low impurity retention, but only if particles can effectively escape the last closed flux surface. We speculate that the lack of strong main ion density gradients in the pedestal prevent the formation of a neoclassical inward pinch, but further experimentation and analysis is needed to confirm this hypothesis.

It is worth highlighting that the flat or hollow nature of core impurity density profiles is strongly constrained by C^{6+} measurements (*c.f.* Fig. 4). While these are not free of modeling assumptions (e.g. taking $n = 2$ halo contributions to be negligible) and uncertainties (e.g. in

the atomic rates and beam attenuation coefficients), the constraint that CER data provide on the C profile shape is believed to be robust. Previous research on experimental impurity transport inferences highlighted difficulties in reproducing flat or hollow impurity profiles on Alcator C-Mod [36] and AUG [64]. In the present work, nonlinear CGYRO simulations have been shown to appropriately reproduce observations of near-flat impurity profiles, whereas quasilinear gyrofluid TGLF runs often over-predict profile peakedness. Scans of TGLF inputs within experimental uncertainties, similar to those in Ref. [35], show that D and v can only be determined within $\approx 50\%$ of their nominal values in the $\delta < 0$ discharges, given current measurement uncertainties. As shown in Appendix A, the difference in D and v predictions from different TGLF saturation rules is typically comparable to this uncertainty. However, TGLF SAT-2 generally tends to give larger (and more trustworthy) estimates closer to the edge, predicting larger diffusion and convection components, which balance to give a relatively consistent v/D (profile peaking). This suggests that profile peakedness does not offer sufficient constraints to experimentally discriminate between saturation models, whereas separate D and v radial profiles, as estimated in this work, are important.

Future work using the `ImpRad` *multi-impurity* framework will compare inferred D and v for each species with theoretical modeling, attempting to quantify Z scalings for neoclassical transport near the magnetic axis (where impurity accumulation can be particularly damaging) and in the pedestal. Investigations into CER measurements of multiple impurity charge states, similarly to AUG work in Refs. [46, 65], are ongoing.

7. Conclusion

The negative triangularity discharges described in this paper clearly offer a valuable foundation for further tokamak scenario development. Experimental results from diverted $\delta < 0$ discharges demonstrate favorable (rapid) impurity transport at $\delta < 0$ in DIII-D. They also appear to confirm the overall applicability of currently-available theoretical transport models, based on application of neoclassical, quasilinear gyrofluid, and nonlinear gyrokinetic models in this work. Theoretical predictions for impurity transport coefficients have been compared with the results of an advanced framework for experimental inferences based on LBO injections, implemented in the OMFIT `ImpRad` module. Radial profiles of D and v from nonlinear CGYRO simulations have been found to match well with experimental results, whereas non-negligible discrepancies have been highlighted for TGLF SAT-2.

Given the high performance and low impurity retention achieved at $\delta < 0$, it appears possible that a high-field device running in L-mode at $\delta < 0$ could offer highly-radiative scenarios and considerable advantages for divertor operation. DIII-D diverted $\delta < 0$ operation with a reinforced outer wall in 2022 will further investigate this promising scenario.

Acknowledgements

The authors would like to thank the entire DIII-D Team, particularly all those involved in diverted negative triangularity experiments. FS is thankful to R. Dux, A. G. McLean, and A. Bortolon for conversations on impurity transport and spectroscopy; to G. M. Staebler, E. A. Belli, J. Candy, and T. Neiser for help with theory models; to T. Pütterich and E. Fable for considerations on tokamak scenarios; and to M. O'Mullane for continuous support with ADAS data. This work made use of the OMFIT framework¶; the authors are grateful to all those who have contributed to its development. Simulations in this paper were run on the *engaging* cluster at the MGHPCC facility, funded by DoE award No. DE-FG02-91-ER54109, as well as the National Energy Research Scientific Computing Center (NERSC)—a US DoE Office of Science User Facility operated under Contract No. DE-AC02-05CH11231. This material is based upon work supported by the Department of Energy under award numbers DE-SC0014264, DE-FC02-04ER54698, DE-AC05-00OR22725, and DE-SC0007880.

¶ <https://omfit.io/>

Appendices

A. Comparison of Particle Transport Predictions via different TGLF Quasilinear Saturation Rules

In order to compare impurity D and v from different TGLF saturation rules, we run the code with trace species (in concentration of 10^{-6} , as in CGYRO) and modify background gradients from nominal values. As described in numerous previous works (e.g. Refs. [35, 66, 67, 30]), this allows one to separate various convection components that have clear physical interpretations as

$$\begin{aligned} \frac{R\Gamma_z}{n_z} &= D_z \frac{R}{L_{n,z}} + D_{T,z} \frac{R}{L_{T,z}} + D_{u,z} \frac{R}{v_{th}} \frac{\partial\Omega_\phi}{\partial r} + Rv_{p,z} \\ &= D_z \frac{R}{L_{n,z}} + Rv_{T,z} + Rv_{\text{rot},z} + Rv_{p,z} \end{aligned} \quad (1)$$

Here we have separated the usual diagonal diffusion, D_z , from a thermodiffusion term, $D_{T,z}$, a rotodiffusion term, $D_{u,z}$, and a pure convection term $v_{p,z}$ (z subscripts will be dropped henceforth). For clarity, in the second line we have also defined $v_T := D_T/L_T$ and $v_u := D_u \frac{1}{v_{th}} \frac{\partial\Omega_\phi}{\partial r}$, which have units of m/s and are more easily identified as thermal and rotational convection term. To quantify each of the convection terms, we introduce trace species in each TGLF run. Relative to the main-ion density, we vary by a small percentage the input density gradient of the second, third, and fourth trace species; the input temperature gradient of the third and fourth species; and the input rotation gradient of the fourth species. Since the TGLF numerical cost scales with the number of species squared, in practice we run TGLF multiple times with a single trace impurity, thus computing each term (all with an implied z subscript) of the following equation:

$$\frac{R}{n} \begin{pmatrix} \Gamma_1 \\ \Gamma_2 \\ \Gamma_3 \\ \Gamma_4 \end{pmatrix} = \begin{pmatrix} R/L_n & R/L_T & R/L_u & 1 \\ R/L_{n,\text{mod}} & R/L_T & R/L_u & 1 \\ R/L_n & R/L_{T,\text{mod}} & R/L_u & 1 \\ R/L_n & R/L_T & R/L_{u,\text{mod}} & 1 \end{pmatrix} \begin{pmatrix} D \\ v_T \\ v_u \\ v_p \end{pmatrix}. \quad (2)$$

By inverting the matrix in Eq. 2, one can then compute D , v_T , v_u , and v_p . Such decomposition is independent of the transport model, and analogous calculations have also been made for the NEO and CGYRO calculations described in Section 5), omitting the thermodiffusion and rotodiffusion terms. The same matrix inversion is of course also applicable for different TGLF saturation rules. Figs. 15 (#180520), 16 (#180526) and 17 (#180530) show comparisons of the transport coefficients computed with TGLF SAT-0 (continuous lines), SAT-1 (dashed lines), and SAT-2 (dash-dotted lines) for the three $\delta < 0$ discharges discussed in detail in this paper. Different colors in the center and lower panels identify components of v and v/D related to the pure pinch, thermodiffusion, rotodiffusion, and a total over all these (only the total can be compared to experimental inferences).

Whereas the TGLF D and v results compared to experimental inferences in Figs. 12, 11 and 13 were computed from background profiles that were iteratively modified via TGYRO in order to match heat and particle fluxes, the results displayed here used the nominal experimental plasma description as resulting from TRANSP runs, since the flux matching process would differ for different TGLF saturation rules.

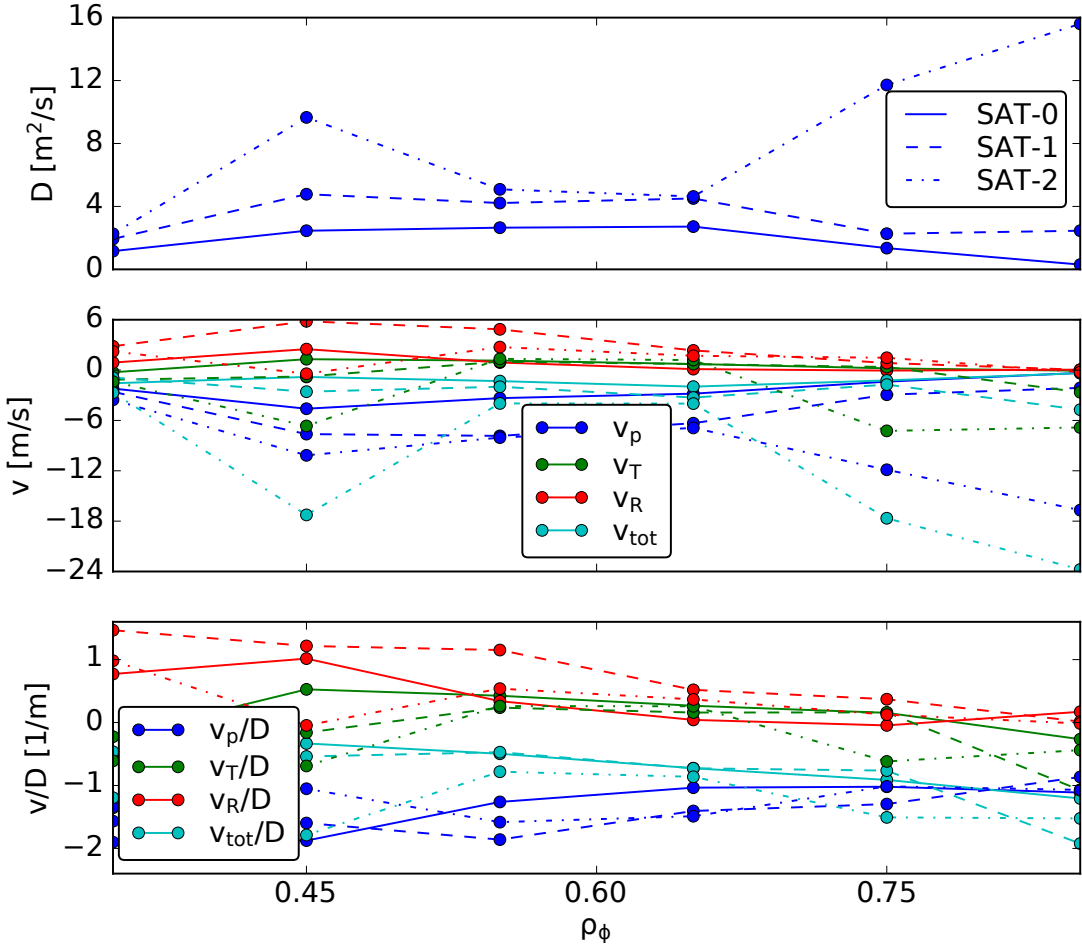


Figure 15: Comparison of particle transport predictions in the low-power H-mode case (#180520) by SAT-0, SAT-1, and SAT-2 saturation rules of TGLF, separating pure pinch, thermodiffusion and rotodiffusion components in the convection coefficient.

These figures lend themselves to some interesting observations. First, it is evident that SAT-2 always predicts larger D values than SAT-1, which gives yet larger D than SAT-0. SAT-2 appears to be most sensitive to background details, resulting in strong radial variations rather than smooth D profiles. Focusing on the v and v/D panels, one notices that thermodiffusion is approximately consistent across the three saturation rules, with v_T

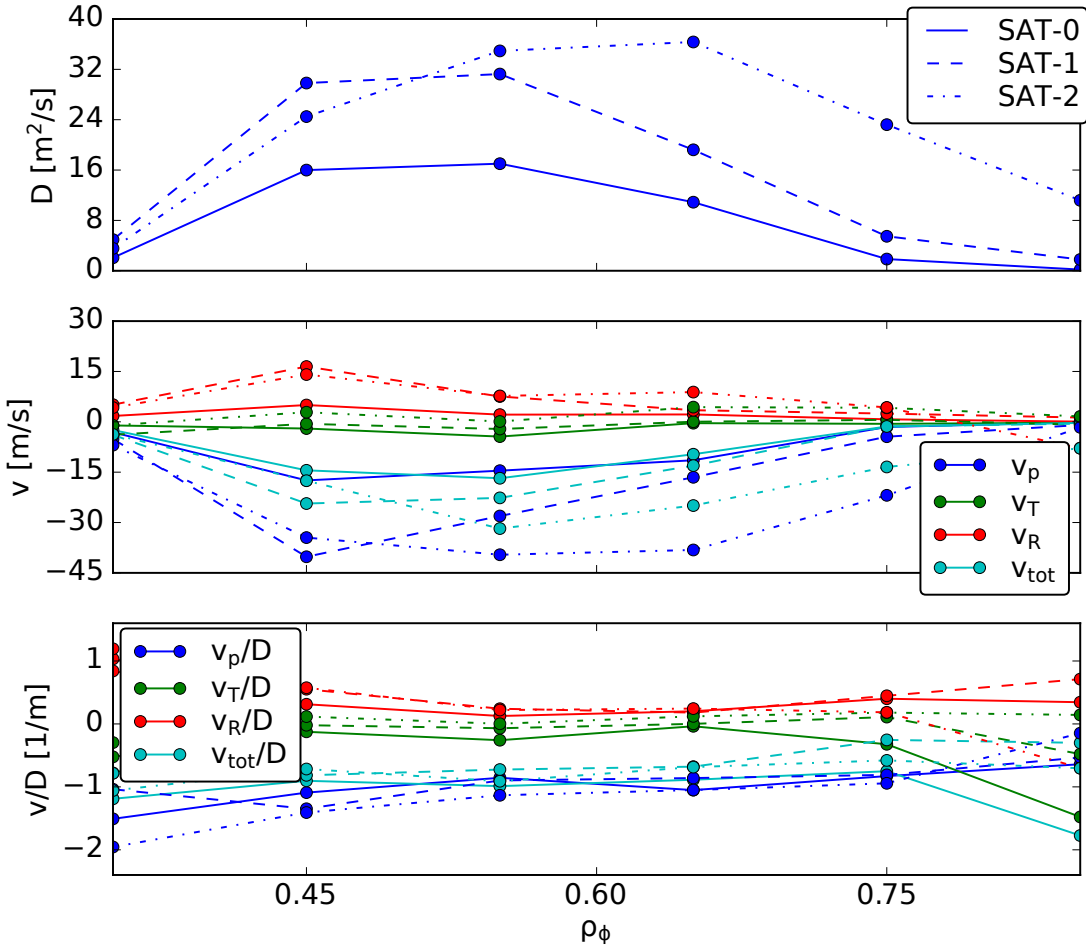


Figure 16: Comparison of particle transport predictions in the low-power L-mode case (#180526) by SAT-0, SAT-1, and SAT-2 saturation rules of TGLF, separating pure pinch, thermodiffusion and rotodiffusion components in the convection coefficient.

values generally being small in the discharges examined here; differences in v_T are amplified in v/D due to large variations in D . One may also remark that SAT-0 predicts lower rotodiffusion than the other two models, corresponding to a smaller dependency on rotation gradients with respect to more recent saturation rules. SAT-2 is found to always predict larger D and v_{tot} in the outer part of the plasma, where it is designed to provide important improvements with respect to older saturation models. This, however, does not lead to significantly different v/D (density peaking).

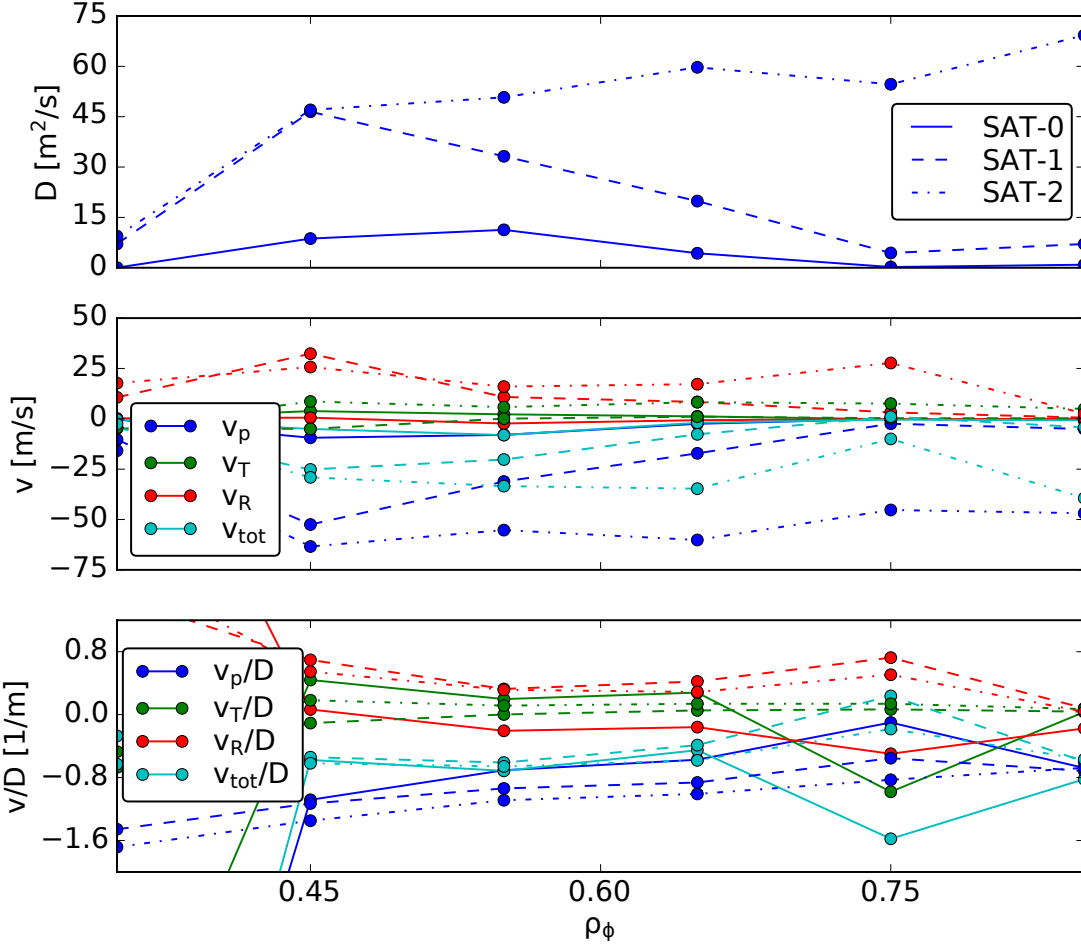


Figure 17: Comparison of particle transport predictions in the high-power L-mode case (#180530) by SAT-0, SAT-1, and SAT-2 saturation rules of TGLF, separating pure pinch, thermodiffusion and rotodiffusion components in the convection coefficient.

B. Effects of NBI CX on Impurity Ionization Equilibrium

On tokamaks that make use of Neutral Beam Injection (NBI), beams constitute an additional source of neutrals in the plasma. Unlike edge neutrals, NBI neutrals have both a fast and a thermal population. The fast population can be separated into three components, typically labelled “full-”, “half-” and “third-” energy. This nomenclature reflects the fact that these neutral populations are created in the NBI beam duct by the application of a single (nominal) accelerating voltage. Such voltage acts on ionized D^+ atoms, D_2^+ molecules or D_3^+ molecules. Each of these is accelerated to the same energy, before being neutralized again so as to be able to penetrate across the tokamak magnetic field. For a fixed energy, each ion has a speed

that depends on its mass. Once the molecular ions dissociate in either the neutralizer cell or in the plasma, the resulting individual D neutrals have an energy that corresponds to the original speed from the acceleration process, giving full, half and one third energies for the D, D_2 and D_3 populations, respectively. Upon entering the plasma, the NBI fast D neutrals can undergo CX reactions, causing recombination of D ions into thermal neutrals that can undergo CX once more. Multiple “generations” of CX can thus be produced. The first generation is affected by CX cross sections involving a fast neutral; all following generations only involve thermal particles. Thermal neutrals produced by the NBI are collectively called “halos”, since they surround the fast beam. To compute the spatial distribution of beam neutrals (both fast and thermal), we make use of the FIDASIM Monte Carlo code [68, 50]. FIDASIM is a state-of-the-art numerical tool that takes as inputs the plasma background (kinetic profiles, plasma geometry, etc.) and beam parameters, adopting a comprehensive collisional-radiative model to account for ionization and recombination processes of neutrals. On both DIII-D [69, 70] and AUG [71] FIDASIM is used to accurately model emission from ions that can undergo charge transfer with NBI neutrals.

In this appendix, we investigate the extent to which NBI neutrals may affect impurity ions, focusing on the DIII-D diverted negative triangularity discharge #180526 (the low-power L-mode case considered in the main body of this paper). Since F impurities were injected via LBO into this discharge, we focus on F ions as an example. Similar analysis has been completed for all the DIII-D discharges analyzed in this paper, looking individually at all beams operating in each case. In shot #180526, two beams (“30L” and “33L”) were active at $t = 2.75$ s, when the LBO injection occurred. Fig. 18 shows the density of the full-energy component of the 30L beam neutral population over the poloidal cross section. The blue contours represent flux surfaces, with the thicker blue line identifying the LCFS. The 30L beam neutrals are seen to penetrate through the center of the plasma and into the HFS.

Based on Fig. 18, one may expect CX between impurities and beam neutrals to be mostly a phenomenon of edge relevance, since the neutral density is clearly higher in the edge. This is however not the case. As discussed in Section ??, CX reactions are effectively averaged out over flux surfaces and, since differential volumes between flux surfaces increase as one goes further out in radius, their relevance is greater in the core region. Fig. 19 shows the flux surface averaged (FSA) density of full-energy (fdens), half-energy (hdens) and third-energy (tdens) components, as well as the sum over all the halo generations, for the 30L beam in shot #180526. Results for the first 3 excited states of neutrals are displayed. We remark that the $n = 1$ halo density is approximately twice as large as the full-energy component density.

Fig. 20 shows the charge exchange recombination rates of an ion of charge $Z = 9$ with each of the beam neutral populations. To compute these, we used rates from Janev & Smith [72] for fast neutrals and the ADAS thermal charge exchange rates for halos (the same used for edge thermal neutrals). For impurity transport simulations, similar calculations are

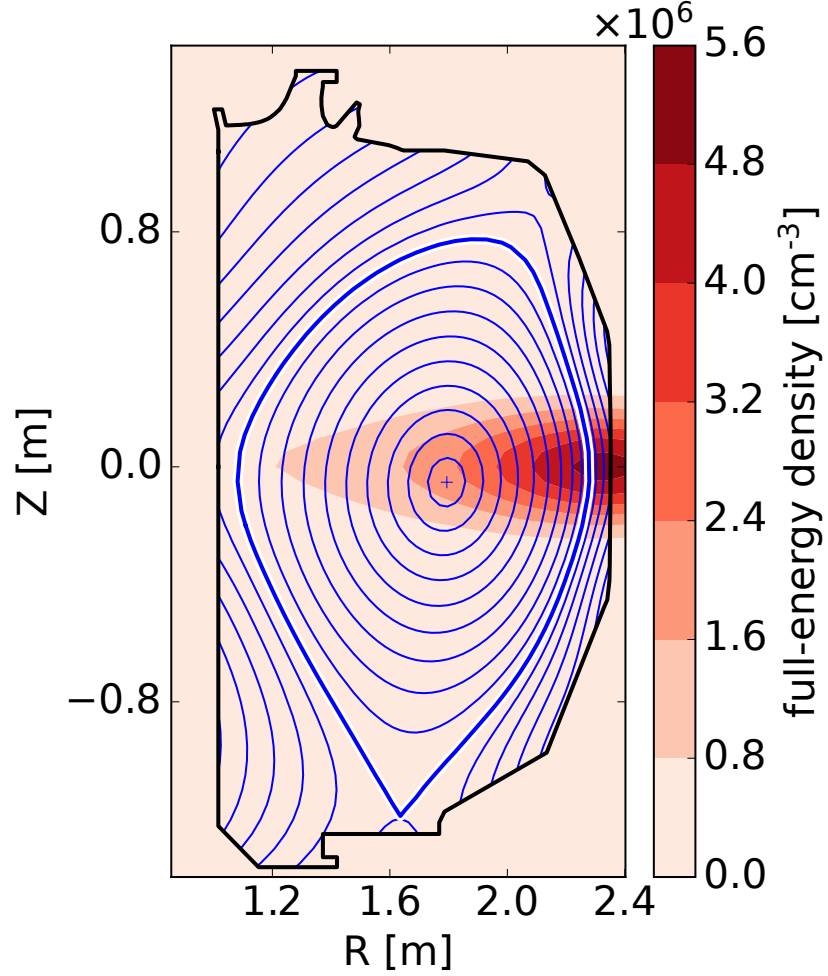


Figure 18: Density of the full-energy fast neutral beam component incident from the right hand (low-field) side, displayed over the poloidal cross section of the DIII-D negative triangularity discharge #180526. Contours of the ρ_p coordinate identify selected flux surfaces, with the thick white line showing the LCFS.

needed for all charge states.

Fig. 21 compares the total recombination rate from all NBI neutrals from beam 30L (fast and thermal) with those from radiative recombination (RR) and dielectronic recombination (DR). The latter two processes give much larger rates near the edge, but are of similar magnitude to the NBI CXR near the magnetic axis. Since both the 30L and 33L beams were active at the simulated time of interest in this discharge, CXR from both must be considered. For $q = 9$ (e.g. fully-stripped F), this brings the total CXR rate to approximately 10.8 s^{-1} in shot #180526 at 2.75 s, which is approximately a factor of 2 larger than the sum of RR and DR on axis.

However, it is important to compare these values with those of ionization rates, S ,

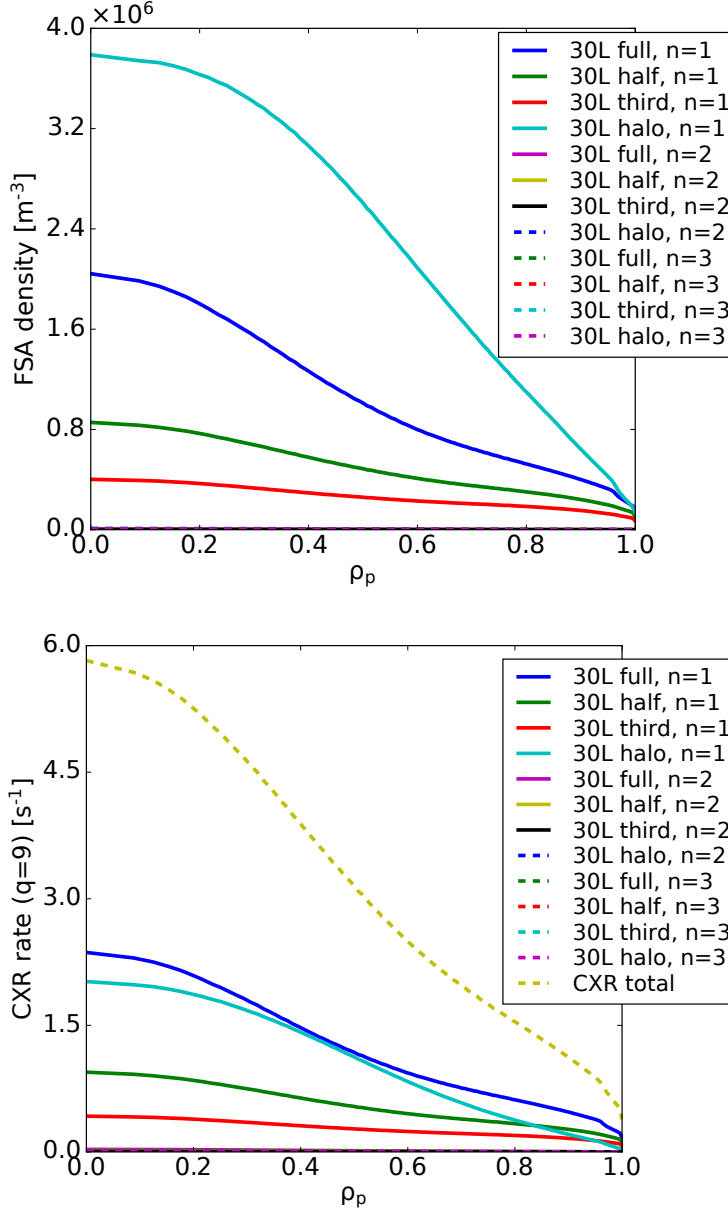


Figure 19: FSA density components from FIDASIM for the DIII-D discharge of Fig. 18, separating full-, half- and third-energy components of fast neutrals and thermal (halo) contributions. Terms arising from the $n = 1$ (ground state) and excited states $n = 2$ and $n = 3$ are separated.

Figure 20: Radial profiles of recombination for F^{9+} ions due to CX with high energy and thermal (halo) neutrals from the DIII-D 30L beam in shot #180526. Contributions from excited states are found to be small.

shown in Fig. 9. Since core plasmas are in a strongly ionizing regime, the modification of total recombination rates due to CX between impurities and NBI neutrals does not have a major impact in forward modeling. Impurity transport in DIII-D may therefore, to a good approximation, be analyzed without considering the effects of NBI neutrals on the impurity charge state balance. High fidelity modeling must, however, examine NBI CXR on a case-by-case basis, since it hard to generalize how NBI CXR balances with other recombination rates for a given ion of interest.

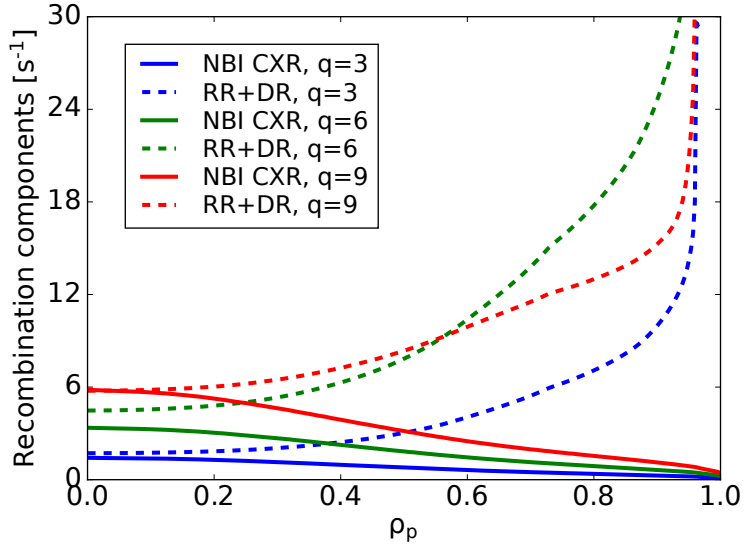


Figure 21: Illustration of the total impact of CX between NBI neutrals and low-Z ions, specifically for F^{3+} , F^{6+} and F^{9+} , summing over all fast and thermal components, ground and excited states 1-3, of beam 30L in the DIII-D discharge #180526.

- [1] F. Wagner, G. Becker, K. Behringer, D. Campbell, and and others. Regime of Improved Confinement and High Beta in Neutral-Beam-Heated Divertor Discharges of the ASDEX Tokamak. *Physical Review Letters*, 49(19):1179–1068, 1982.
- [2] D. Silvagni, T. Eich, M. Faitsch, T. Happel, B. Sieglin, P. David, D. Nille, L. Gil, U. Stroth, the ASDEX Upgrade team, and the EUROfusion MST1 team. Scrape-off layer (SOL) power width scaling and correlation between SOL and pedestal gradients across L, I and H-mode plasmas at ASDEX Upgrade. *Plasma Physics and Controlled Fusion*, 62(4):045015, 2 2020.
- [3] S. Yu Medvedev, M. Kikuchi, L. Villard, T. Takizuka, P. Diamond, H. Zushi, K. Nagasaki, X. Duan, Y. Wu, A. A. Ivanov, A. A. Martynov, Yu Yu Poshekhanov, A. Fasoli, and O. Sauter. The negative triangularity tokamak: Stability limits and prospects as a fusion energy system. *Nuclear Fusion*, 55(6), 2015.
- [4] M Kikuchi, T Takizuka, S Medvedev, T Ando, D Chen, J X Li, M. Austin, O. Sauter, L. Villard, A. Merle, M. Fontana, Y. Kishimoto, and K. Imadera. L-mode-edge negative triangularity tokamak reactor. *Nuclear Fusion*, 59(5), 2019.
- [5] Y Camenen, A Pochelon, R Behn, A Bottino, A Bortolon, S Coda, A Karpushov, O Sauter, and G. Zhuang. Impact of plasma triangularity and collisionality on electron heat transport in TCV L-mode plasmas. In *Nuclear Fusion*, volume 47, pages 510–516. IOP Publishing, 6 2007.
- [6] S. Coda et al. Physics research on the TCV tokamak facility: From conventional to alternative scenarios and beyond. *Nuclear Fusion*, 59(11):112023, 8 2019.
- [7] J. L. Luxon. A design retrospective of the DIII-D tokamak. *Nuclear Fusion*, 42(5):614–633, 5 2002.
- [8] M. E. Austin, A. Marinoni, M. L. Walker, M. W. Brookman, J. S. Degrassie, A. W. Hyatt, G. R. McKee, C. C. Petty, T. L. Rhodes, S. P. Smith, C. Sung, K. E. Thome, and A. D. Turnbull. Achievement of Reactor-Relevant Performance in Negative Triangularity Shape in the DIII-D Tokamak. *Physical Review Letters*, 122(11):115001, 2019.
- [9] A. Marinoni, M. E. Austin, A W Hyatt, M L Walker, J Candy, C Chrystal, C J Lasnier, G. R. McKee, T. Odstrčil, C. C. Petty, M. Porkolab, J. C. Rost, O Sauter, S. P. Smith, G. M. Staebler, C. Sung, K. E. Thome, A D Turnbull, and L. Zeng. H-mode grade confinement in L-mode edge plasmas at negative triangularity on DIII-D. *Physics of Plasmas*, 26(4), 2019.
- [10] A. Marinoni, M.E. Austin, A.W. Hyatt, S. Saarelma, F. Scotti, Z. Yan, C. Chrystal, S. Coda, F. Glass, J.M. Hanson, A.G. McLean, D.C. Pace, C. Paz-Soldan, C.C. Petty, M. Porkolab, L. Schmitz, F. Sciortino, S.P. Smith, K.E. Thome, F. Turco, and the DIII-D Team. Diverted negative triangularity plasmas on DIII-D: the benefit of high confinement without the liability of an edge pedestal. *Nuclear Fusion*, 61(11):116010, 9 2021.
- [11] S Saarelma, M E Austin, M Knolker, A Marinoni, C Paz-Soldan, L Schmitz, and P B Snyder. Ballooning instability preventing the H-mode access in plasmas with negative triangularity shape on the DIII-D tokamak. *Plasma Physics and Controlled Fusion*, 63(10):105006, 9 2021.
- [12] C Paz-Soldan. Plasma performance and operational space without ELMs in DIII-D. *Plasma Physics and Controlled Fusion*, 63(8):83001, 2021.
- [13] A. Marinoni, S. Brunner, Y. Camenen, S. Coda, J. P. Graves, X. Lapillon, A. Pochelon, O. Sauter, and L. Villard. The effect of plasma triangularity on turbulent transport: Modeling TCV experiments by linear and non-linear gyrokinetic simulations. *Plasma Physics and Controlled Fusion*, 51(5), 2009.
- [14] M. Fontana, L. Porte, S. Coda, and O. Sauter. The effect of triangularity on fluctuations in a tokamak plasma. *Nuclear Fusion*, 58(2), 2018.
- [15] W. Han, N. Offeddu, T. Golfinopoulos, C. Theiler, C. K. Tsui, J. A. Boedo, E. S. Marmar, and TCV Team. Suppression of first-wall interaction in negative triangularity plasmas on TCV. *Nuclear Fusion*, 61(034003), 2021.
- [16] F Sciortino. Experimental inference of particle transport in tokamak plasmas. 2021.
- [17] L. L. Lao, H. St John, R. D. Stambaugh, A. G. Kellman, and W. Pfeiffer. Reconstruction of current profile parameters and plasma shapes in tokamaks. *Nuclear Fusion*, 25(11):1611–1622, 1985.
- [18] P. N. Yushmanov, P. N. Yushmanov, T. Takizuka, K. S. Riedel, O. J.W.F. Kardaun, J. G. Cordey, S. M.

- Kaye, and D. E. Post. Scalings for tokamak energy confinement. *Nuclear Fusion*, 30(10):1999–2006, 10 1990.
- [19] W. Horton, D. I. In Choi, and W. M. Tang. Toroidal drift modes driven by ion pressure gradients. *Physics of Fluids*, 24(6):1077–1085, 6 1981.
 - [20] P. Ennever, M. Porkolab, J. Candy, G. Staebler, M. L. Reinke, J. E. Rice, J. C. Rost, D. Ernst, C. Fiore, J. Hughes, and J. Terry. The effects of dilution on turbulence and transport in C-Mod ohmic plasmas and comparisons with gyrokinetic simulations. *Physics of Plasmas*, 22(7):072507, 7 2015.
 - [21] B B Kadomtsev and O P Pogutse. Plasma instability on trapped particles in a toroidal geometry. *Zh. Eksp. Teor. Fiz.*, 1734-46(51), 1966.
 - [22] A. W. Leonard, W. H. Meyer, B. Geer, D. M. Behne, and D. N. Hill. 2D tomography with bolometry in DIII-Da). *Review of Scientific Instruments*, 66(2):1201–1204, 6 1995.
 - [23] ITER Physics Expert Group on Confinement and Transport. Chapter 2: Plasma confinement and transport Interval estimation of global H-mode energy confinement in ITER. *Nuclear Fusion*, 39(2175), 1999.
 - [24] D. G. Whyte, A. E. Hubbard, J. W. Hughes, B. Lipschultz, J. E. Rice, E. S. Marmar, M. Greenwald, I. Cziegler, A. Dominguez, T. Golfinopoulos, N. Howard, L. Lin, R. M. McDermott, M. Porkolab, M. L. Reinke, J. Terry, N. Tsujii, S. Wolfe, S. Wukitch, and Y. Lin. I-mode: An H-mode energy confinement regime with L-mode particle transport in Alcator C-Mod. *Nuclear Fusion*, 50(10):105005, 2010.
 - [25] J. E. Rice, M. L. Reinke, C. Gao, N. T. Howard, M. A. Chilenski, L. Delgado-Aparicio, R. S. Granetz, M. J. Greenwald, A. E. Hubbard, J. W. Hughes, J. H. Irby, Y. Lin, E. S. Marmar, R. T. Mumgaard, S. D. Scott, J. L. Terry, J. R. Walk, A. E. White, D. G. Whyte, S. M. Wolfe, and S. J. Wukitch. Core impurity transport in Alcator C-Mod L-, I- and H-mode plasmas. *Nuclear Fusion*, 55(3):033014, 2015.
 - [26] A. Marinoni, J. C. Rost, M. Porkolab, A. E. Hubbard, T. H. Osborne, A. E. White, D. G. Whyte, T. L. Rhodes, E. M. Davis, D. R. Ernst, and K. H. Burrell. Characterization of density fluctuations during the search for an I-mode regime on the DIII-D tokamak. *Nuclear Fusion*, 55(9):93019, 2015.
 - [27] F. Sciortino, T. Odstrčil, A. Cavallaro, S P Smith, O. Meneghini, R. Reksoatmodjo, O. Linder, J. D. Lore, N. T. Howard, E. S. Marmar, and S. Mordijk. Modeling of particle transport, neutrals and radiation in magnetically-confined plasmas with Aurora. *Plasma Physics and Controlled Fusion*, 63(11):112001, 9 2021.
 - [28] T. Odstrčil, T. Puettnerich, R. Bilato, M. Weiland, A. Gude, and D. Mazon. Investigation of the fast particle velocity space by diagnosing poloidal asymmetries of heavy ions at ASDEX Upgrade. In *43rd European Physical Society Conference on Plasma Physics, EPS 2016*, number 1, pages 1–4, 2016.
 - [29] C. Angioni, P. Mantica, T. Pütterich, M. Valisa, M. Baruzzo, E. A. Belli, P. Belo, F. J. Casson, C. Challis, P. Drewelow, C. Giroud, N. Hawkes, T. C. Hender, J. Hobirk, T. Koskela, L. Lauro Taroni, C. F. Maggi, J. Mlynar, T. Odstrčil, M. L. Reinke, and M. Romanelli. Tungsten transport in JET H-mode plasmas in hybrid scenario, experimental observations and modelling. *Nuclear Fusion*, 54(8):083028, 2014.
 - [30] C. Angioni. Impurity transport in tokamak plasmas, theory, modelling and comparison with experiments. *Plasma Physics and Controlled Fusion*, 63(7):073001, 2021.
 - [31] J. Skilling. Nested sampling for general Bayesian computation. *Bayesian Analysis*, 1(4):833–860, 2006.
 - [32] F. Feroz and M. P. Hobson. Multimodal nested sampling: An efficient and robust alternative to Markov Chain Monte Carlo methods for astronomical data analyses. *Monthly Notices of the Royal Astronomical Society*, 384(2):449–463, 2008.
 - [33] F. Feroz, M. P. Hobson, E. Cameron, and A. N. Pettitt. Importance Nested Sampling and the MultiNest Algorithm. *arXiv*, pages 1–28, 2013.
 - [34] F. Sciortino, N. M. Cao, N. T. Howard, E. S. Marmar, and J. E. Rice. Particle transport constraints via Bayesian spectral fitting of multiple atomic lines. *Review of Scientific Instruments*, 92:53508, 2021.
 - [35] F. Sciortino, N. T. Howard, E S. Marmar, T. Odstrčil, N. M Cao, R. Dux, A. E Hubbard, J. W Hughes,

- J. H Irby, Y. M. Marzouk, L. M. Milanese, M. L. Reinke, J. E Rice, and P. Rodriguez-Fernandez. Inference of experimental radial impurity transport on Alcator C-Mod: Bayesian parameter estimation and model selection. *Nuclear Fusion*, 60(12), 8 2020.
- [36] Francesco Sciortino, Nathan T Howard, Richard Reksoatmodjo, Adam Robert Foster, Jerry W Hughes, Earl S Marmar, Marco Andres Miller, Saskia Mordijk, T. Odstrčil, Thomas Pütterich, Matthew L Reinke, John E Rice, and Pablo Rodriguez-Fernandez. Experimental inference of neutral and impurity transport in alcator C-mod using high-resolution X-ray and ultra-violet spectra. *Nuclear Fusion*, 61(12):126060, 11 2021.
- [37] B. A. Grierson, K. H. Burrell, R. M. Nazikian, W. M. Solomon, A. M. Garofalo, E. A. Belli, G. M. Staebler, M. E. Fenstermacher, G. R. McKee, T. E. Evans, D. M. Orlov, S. P. Smith, C. Chrobak, and C. Chrystal. Impurity confinement and transport in high confinement regimes without edge localized modes on DIII-D. *Physics of Plasmas*, 22(5):055901, 2015.
- [38] B. S. Victor, T. Odstrčil, C. A. Paz-Soldan, B. A. Grierson, E. Hinson, A. Jarvinen, E. M. Hollmann, C. Chrystal, C. S. Collins, K. E. Thome, and S. L. Allen. Impurity transport in the pedestal of H-mode plasmas with resonant magnetic perturbations. *Plasma Physics and Controlled Fusion*, 62(9):095021, 9 2020.
- [39] T. Odstrčil, N. T. Howard, F. Sciortino, C. Chrystal, C. Holland, E. Hollmann, G. McKee, K. E. Thome, and T. M. Wilks. Dependence of the impurity transport on the dominant turbulent regime in ELM-y H-mode discharges on the DIII-D tokamak. *Physics of Plasmas*, 27(8):082503, 8 2020.
- [40] J. H. Yu, J. A. Boedo, E. M. Hollmann, R. A. Moyer, D. L. Rudakov, and P. B. Snyder. Fast imaging of edge localized mode structure and dynamics in DIII-D. *Physics of Plasmas*, 15(3):032504, 3 2008.
- [41] E. S. Marmar, J. L. Cecchi, and S. A. Cohen. System for rapid injection of metal atoms into plasmas. *Review of Scientific Instruments*, 46(9):1149–1154, 1975.
- [42] R. J. Fonck, A. T. Ramsey, and R. V. Yelle. Multichannel grazing-incidence spectrometer for plasma impurity diagnosis: SPRED. *Applied Optics*, 21(12):2115, 1982.
- [43] A. Kramida, Yu. Ralchenko, J. Reader, and and NIST ASD Team. NIST Atomic Spectra Database (ver. 5.8), [Online]. Available: <https://physics.nist.gov/asd> [2021, May 26]. National Institute of Standards and Technology, Gaithersburg, MD., 2020.
- [44] E. M. Hollmann, L. Chousal, R. K. Fisher, R. Hernandez, G. L. Jackson, M. J. Lanctot, S. V. Pidcoe, J. Shankara, and D. A. Taussig. Soft x-ray array system with variable filters for the DIII-D tokamak. *Review of Scientific Instruments*, 82(11):113507, 11 2011.
- [45] E. A. Belli and J. Candy. Kinetic calculation of neoclassical transport including self-consistent electron and impurity dynamics. *Plasma Physics and Controlled Fusion*, 50(9):0–32, 2008.
- [46] R. Dux, M. Cavedon, A. Kallenbach, R. M. McDermott, G. Vogel, and The Asdex Upgrade Team. Influence of CX-reactions on the radiation in the pedestal region at ASDEX Upgrade. *Nuclear Fusion*, 60(12), 2020.
- [47] Xavier Bonnin, Wouter Dekeyser, Richard Pitts, David Coster, Serguey Voskoboinikov, and Sven Wiesen. Presentation of the New SOLPS-ITER Code Package for Tokamak Plasma Edge Modelling. *Plasma and Fusion Research*, 11:1–6, 2016.
- [48] S. Wiesen, D. Reiter, V. Kotov, M. Baelmans, W. Dekeyser, A. S. Kukushkin, S. W. Lisgo, R. A. Pitts, V. Rozhansky, G. Saibene, I. Veselova, and S. Voskoboinikov. The new SOLPS-ITER code package. *Journal of Nuclear Materials*, 463:480–484, 7 2015.
- [49] D. Reiter, M. Baelmans, and P. Börner. The eirene and B2-eirene codes. *Fusion Science and Technology*, 47(2):172–186, 2005.
- [50] B. Geiger, L. Stagner, W.W. Heidbrink, R. Dux, R. Fischer, Y. Fujiwara, and And Others. Progress in modelling fast-ion D-alpha spectra and neutral particle analyzer fluxes using FIDASIM. *Plasma Physics and Controlled Fusion*, 2019.
- [51] L. Stagner, B. Geiger, and W.W. Heidbrink. FIDASIM: A Neutral Beam and Fast-ion Diagnostic Modeling Suite.
- [52] M. E. Austin and J. Lohr. Electron cyclotron emission radiometer upgrade on the DIII-D tokamak. In

- Review of Scientific Instruments*, volume 74, pages 1457–1459. American Institute of PhysicsAIP, 3 2003.
- [53] F. H. Seguin, R. Petrasso, and E. S. Marmar. Effects of Internal Disruptions on Impurity Transport in Tokamaks. *Physical Review Letters*, 51(6):455–458, 8 1983.
 - [54] E. A. Belli and J. Candy. Full linearized Fokker-Planck collisions in neoclassical transport simulations. *Plasma Physics and Controlled Fusion*, 54(1):015015, 1 2012.
 - [55] G M Staebler, J E Kinsey, and R E Waltz. A theory-based transport model with comprehensive physics. In *Physics of Plasmas*, volume 14, page 055909, 2007.
 - [56] G. M. Staebler, J. Candy, N. T. Howard, and C. Holland. The role of zonal flows in the saturation of multi-scale gyrokinetic turbulence. *Physics of Plasmas*, 23(6), 2016.
 - [57] G. M. Staebler, J. Candy, E. A. Belli, J. E. Kinsey, N. Bonanomi, and B. Patel. Geometry dependence of the fluctuation intensity in gyrokinetic turbulence. *Plasma Physics and Controlled Fusion*, 63(1):015013, 11 2020.
 - [58] J. Candy, E. A. Belli, and R. V. Bravenec. A high-accuracy Eulerian gyrokinetic solver for collisional plasmas. *Journal of Computational Physics*, 324:73–93, 2016.
 - [59] J. Candy, C. Holland, R. E. Waltz, M. R. Fahey, and E. Belli. Tokamak profile prediction using direct gyrokinetic and neoclassical simulation. *Physics of Plasmas*, 16(6), 2009.
 - [60] G.M. Staebler, E. A. Belli, J. Candy, J.E. Kinsey, H. Dudding, and B. Patel. Verification of a quasi-linear model for gyrokinetic turbulent transport. *Nuclear Fusion*, 61(11):116007, 9 2021.
 - [61] J. Breslau, M. Gorelenkova, F. Poli, J. Sachdev, X. Yuan, and USDOE Office of Science. TRANSP, 2018.
 - [62] H. Sugama, T. H. Watanabe, and M. Nunami. Linearized model collision operators for multiple ion species plasmas and gyrokinetic entropy balance equations. *Physics of Plasmas*, 16(11):112503, 2009.
 - [63] M. Kotschenreuther, X. Liu, D. R. Hatch, S. Mahajan, L. Zheng, A. Diallo, R. Groebner, J. C. Hillesheim, C. F. Maggi, C. Giroud, F. Koechl, V. Parail, S. Saarelma, E. Solano, and A. Chankin. Gyrokinetic analysis and simulation of pedestals to identify the culprits for energy losses using ‘fingerprints’. *Nuclear Fusion*, 59(9), 2019.
 - [64] R. M. McDermott et al. Validation of low-z impurity transport theory using boron perturbation experiments at asdex upgrade. *submitted to Nuclear Fusion*.
 - [65] T. Nishizawa et al. Non-parametric inference of impurity transport coefficients in the asdex upgrade tokamak. *submitted*.
 - [66] C. Angioni, Y. Camenen, F. J. Casson, E. Fable, R. M. McDermott, A. G. Peeters, and J. E. Rice. Off-diagonal particle and toroidal momentum transport: A survey of experimental, theoretical and modelling aspects, 2012.
 - [67] F. J. Casson, A. G. Peeters, C. Angioni, Y. Camenen, W. A. Hornsby, A. P. Snodin, and G. Szepesi. Gyrokinetic simulations including the centrifugal force in a rotating tokamak plasma. *Physics of Plasmas*, 17(10), 2010.
 - [68] W. W. Heidbrink. Fast-ion D α measurements of the fast-ion distribution. In *Review of Scientific Instruments*, volume 81, page 10D727. American Institute of PhysicsAIP, 10 2010.
 - [69] S. R. Haskey, B. A. Grierson, L Stagner, K. H. Burrell, C Chrystal, R. J. Groebner, A Ashourvan, and N. A. Pablant. Deuterium charge exchange recombination spectroscopy from the top of the pedestal to the scrape off layer in H-mode plasmas. *Journal of Instrumentation*, 12(10), 2017.
 - [70] S R Haskey, B A Grierson, L Stagner, C Chrystal, A Ashourvan, A Bortolon, M D Boyer, K H Burrell, C Collins, R J Groebner, D H Kaplan, and N A Pablant. Active spectroscopy measurements of the deuterium temperature, rotation, and density from the core to scrape off layer on the DIII-D tokamak, 2018.
 - [71] R. M. McDermott, R. Dux, T. Pütterich, B. Geiger, A. Kappatou, A. Lebschy, C. Bruhn, M. Cavedon, A. Frank, N. D. Harder, and E. Viezzer. Evaluation of impurity densities from charge exchange recombination spectroscopy measurements at ASDEX Upgrade. *Plasma Physics and Controlled Fusion*, 60(9):95007, 2018.

- [72] R. K. Janev and J. J. Smith. Cross Sections for Collisions Processes of Hydrogen Atoms with Electrons, Protons and Multiply Charged Ions. *Nuclear Fusion*, 4:195, 1993.